

Dust rings trap protoplanets on eccentric orbits and get consumed by them

David A. Velasco-Romero^{1*}, Frédéric S. Masset^{2,3}, Alessandro Morbidelli³,
Pablo Benítez-Llambay⁴, Leonardo Krapp^{5,6} and Elena Lega³

¹*Department of Astrophysical Sciences, Princeton University, Princeton, NJ 08544, USA*

²*Instituto de Ciencias Físicas, Universidad Nacional Autónoma de México, Av. Universidad s/n, 62210 Cuernavaca, Mor., Mexico*

³*Université Nice-Sophia Antipolis, CNRS, Observatoire de la Côte d'Azur, Laboratoire Lagrange, CS 34229, 06304 Nice Cedex, France*

⁴*Facultad de Ingeniería y Ciencias, Universidad Adolfo Ibáñez, Av. Diagonal las Torres 2640, Peñalolén, Chile*

⁵*Department of Astronomy and Steward Observatory, University of Arizona, Tucson, Arizona 85721, USA*

⁶*Departamento de Astronomía, Universidad de Concepción, Av. Esteban Iturra s/n Barrio Universitario, Casilla 160-C, Chile*

Accepted XXX. Received YYY; in original form ZZZ

ABSTRACT

We study the orbital evolution and mass growth of protoplanets with masses $M \in [0.1 - 8] M_{\oplus}$ in the vicinity of a dusty ring, using three-dimensional numerical simulations with a two-fluid model and nested-meshes. We find two stable, eccentric orbits that lock the planet in the ring vicinity, thereby inhibiting its migration and allowing it to accrete dust from the ring. One of these orbits has an eccentricity comparable to the aspect ratio of the gaseous disc and has its periastron within the ring, enabling intermittent accretion during each pass. The other orbit has a smaller eccentricity and an apoastron slightly inside the ring. A planet locked at the outer orbit efficiently accretes from the ring and can reach the critical mass for runaway gas accretion on timescales $\gtrsim 10^5$ yr (for a $10 M_{\oplus}$ dust ring at 10 au) while a planet locked at the inner orbit has a slower growth and might not supersede the super-Earth stage over the disc lifetime. While in our runs a low-mass embryo forming within the ring eventually joins the outer orbit, it is likely that the path taken depends on the specific details of the ring. The trapping on the outer orbit arises from an intermittent, strong thermal force at each passage through the ring, where the accretion rate spikes. It is insensitive to uncertainties that plague models considering planets trapped on circular orbits in rings. It is highly robust and could allow a growing planet to follow an expanding ring over large distances.

Key words: planet-disc interactions – protoplanetary discs – planets and satellites: formation – hydrodynamics

1 INTRODUCTION

Dust rings are ubiquitous in continuum millimetre images of protoplanetary discs obtained with ALMA (Huang et al. 2018). Even discs that appear smooth with standard image reconstruction techniques reveal annular substructures when super-resolution techniques are used (Jennings et al. 2022). Their origin is not known. While some are thought to be the result of planet-disc interactions (Zhang et al. 2018; Ziampras et al. 2020), others may have a different origin. Dust is known to accumulate at local pressure maxima (Whipple 1972; Fromang & Nelson 2005; Kretke & Lin 2007; Pinilla et al. 2012). These may occur, for instance, in discs subject to non-ideal MHD effects (Béthune et al. 2017; Krapp et al. 2018), and are accompanied by the formation of thin, narrow rings (Riols & Lesur 2018; Riols et al. 2020). Not all explanations for the existence of narrow rings resort to local pressure maxima. When the pressure profile has a small perturbation, insufficient to create a local maximum, the radial drift of the dust slows down where the pressure gradient is small, resulting in a traffic jam of the inwardly flowing dust that appears as a dusty ring (Rosotti et al. 2016). Traffic jams (hence rings) may also appear at ice lines (Drażkowska & Alibert 2017). Jiang & Ormel (2021) introduce the concept of clumpy rings, that can exist in discs

where the pressure has a smooth, monotonous profile. Clumpy rings are the results of radially localised formation of pebble clumps actively forming planetesimals, that are fed by the settling of pebbles and their incorporation into clumpy structures with dust-to-gas ratio in the midplane larger than unity. They may survive in the absence of a pressure bump, and require to be fed by an inward flow of solids from the outer disc, while they leak solids toward the inner disc at a sizeable fraction of the inflow rate from the outer disc. When the conditions for their survival are met, they usually expand outwards and can survive over evolutionary timescales of the disc.

Given that dusty rings are sweet spots for the formation of planetesimals, it is legitimate to investigate how the growth of a planetary embryo would unfold at a dusty ring. In recent years, there has been significant work addressing the growth and orbital evolution of planetary bodies at dusty rings. We shall present and discuss those in section 5.4. Here, we take into account the radiative feedback due to the diffusion into the ambient gas of the energy released by accretion of pebbles as the planet passes through the ring. Indeed, recent work has highlighted the important role played by thermal disturbances on the orbital evolution of low-mass planet in the vicinity of dusty rings (Chrenko & Chametla 2023; Pierens & Raymond 2024). In general, they tend to excite the planet's eccentricity to values comparable to the aspect ratio of the gaseous disc, so that their growth and orbital

* E-mail: david.velasco@princeton.edu

evolution considerably differs from that obtained assuming a circular orbit at a migration trap in the ring.

The force arising from these disturbances, or thermal force, can dominate the force exerted by the disc for low-mass planets, to the point that the classical Lindblad and corotation torques are largely subdominant, if relevant at all. This happens when the thermal length-scale λ , given by:

$$\lambda = \sqrt{\frac{\chi}{\frac{3}{2}\Omega_K\gamma}} \quad (1)$$

is much smaller than the pressure lengthscale $H = c_s/(\sqrt{\gamma}\Omega_K)$, where Ω_K is the Keplerian angular speed, χ the thermal diffusivity, γ the adiabatic index and c_s the adiabatic sound speed. Estimates of the thermal lengthscale in planet forming regions of protoplanetary discs, at a few astronomical units from the central object, show that it is indeed a minute fraction of the pressure lengthscale (Masset 2017).

The action of thermal forces on an embedded planet with a mass M significantly smaller than the thermal mass $h^3 M_\star$ (M_\star being the mass of the central object and h the aspect ratio of the gaseous disc) depends on the planet's luminosity L . When the luminosity is larger than the critical luminosity L_c given by (Masset 2017)

$$L_c = \frac{4\pi GM\chi\rho_0}{\gamma}, \quad (2)$$

where G is the gravity constant and ρ_0 the gas density at the disc's midplane, thermal forces tend to induce an outward migration (Benítez-Llambay et al. 2015) for circular or low eccentricity planets, while at the same time they tend to excite their eccentricity (Chrenko et al. 2017; Eklund & Masset 2017; Fromenteau & Masset 2019; Velasco Romero et al. 2022; Cornejo et al. 2023). As the eccentricity reaches values smaller, but comparable to the aspect ratio of the disc, the migration is found to revert inwards (Eklund & Masset 2017; Chrenko & Chametla 2023). An early interpretation of this reversal was put forward by Eklund & Masset (2017), who speculated that the (positive) corotation torque was quenched by the relatively large value of the eccentricity (Fendyke & Nelson 2014), and that this effect sufficed to revert the torque balance. Regardless of its origin, this reversal can have a decisive effect on the growth and orbital evolution of a planet: should it occur systematically for planets becoming eccentric at dusty rings, they would migrate inwards and leave the ring, thereby interrupting their growth at a very low mass (Chrenko & Chametla 2023).

This paper is organised as follows: In section 2, we revisit this reversal and shed some light on its physical origin. We show that it is intrinsic to, and explained entirely by the behaviour of the thermal force. This, in turn, will lead us to conceive situations in which migration is not reverted at sizeable eccentricity. We shall see that such conditions may easily be met at the edges of dusty rings. We subsequently resort to numerical simulations to check our expectations. The setup is presented in section 3 and the results in section 4. We then discuss our results in section 5 and conclude in section 6.

2 ON THE THERMAL TORQUE REVERSAL WITH ECCENTRICITY

Let us start by noting that, *when the eccentricity is constant in time*, the time averaged torque can be used to infer the migration rate. The time derivative of the planet's angular momentum $J = M\sqrt{GM_\star a(1-e^2)}$ (a and e being the semi-major axis and

eccentricity of the planet) is indeed:

$$\Gamma = \dot{J} = J \left(\frac{\dot{a}}{2a} - \frac{e\dot{e}}{1-e^2} \right), \quad (3)$$

hence the net torque Γ exerted on the planet scales directly with the migration rate \dot{a} when the second term in the parenthesis of the equation above vanishes.

We therefore proceed to evaluate the thermal torque exerted on a low-mass planet, averaged over one orbital period. We entertain two cases: (i) a regime with a radial excursion smaller than the thermal lengthscale, and (ii) a regime with a radial excursion larger than the thermal lengthscale, but smaller than the aspect ratio. This case can exist when the thermal and pressure length scales are well separated.

Case (i) has been studied in detail by Fromenteau & Masset (2019). We adopt notations similar to theirs. The planet has coordinates (x, y) in a frame centred on the guiding centre of the epicycle (x being directed along the radial direction and y by the azimuthal direction):

$$\begin{aligned} x &= -ea \cos(\Omega_p t) \\ y &= 2ea \sin(\Omega_p t), \end{aligned} \quad (4)$$

where Ω_p is the planet's orbital frequency and t the time since a passage at periastron. We work out the thermal force exerted on the planet to first order in eccentricity. The constant term is the force exerted on a planet in circular orbit, and has expression (Masset 2017, Eq. 109):

$$F_y^{[0]} = 0.644 \frac{x_p^0}{\lambda} F_d, \quad (5)$$

where

$$F_d = \frac{\gamma(\gamma-1)GM(L-L_c)}{2\chi c_s^2} \quad (6)$$

is the drag ($L < L_c$) or thrust ($L > L_c$) that the planet would experience in circumstances in which the shear would be negligible (Velasco Romero & Masset 2019), and $x_p^0 = a - r_c$ is the offset between the semi-major axis and the corotation radius r_c , set by the radial pressure gradient of the gas. In most of the discussion that follows we restrict ourselves to the case $L > L_c$ (i.e. the net thermal force is dominated by the heating of the ambient gas). The first order term in eccentricity is (Fromenteau & Masset 2019):

$$F_x^{[1]} = \frac{a}{\pi\lambda} F_d e \left[f_x^C \cos(\Omega_p t) + f_x^S \sin(\Omega_p t) \right] \quad (7)$$

and

$$F_y^{[1]} = \frac{a}{\pi\lambda} F_d e \left[f_y^C \cos(\Omega_p t) + f_y^S \sin(\Omega_p t) \right], \quad (8)$$

where the coefficients $f_{x,y}^{S,C}$ are given at Eqs. (172–175) of Fromenteau & Masset (2019). The time averaged torque is:

$$\langle \Gamma \rangle = \left\langle (a+x)(F_y^{[0]} + F_y^{[1]}) - yF_x^{[1]} \right\rangle. \quad (9)$$

Using Eqs. (4), (5), (7), (8) and (9) we arrive at:

$$\langle \Gamma \rangle = F_d a \left[0.644 \frac{x_p^0}{\lambda} - 0.58 \frac{ae^2}{\lambda} \right]. \quad (10)$$

We see from this equation that the torque decreases as the eccentricity increases. Writing $x_p^0 = a\eta h^2$, where $\eta = O(1)$ is a dimensionless measure of the offset between corotation and orbit (Masset 2017), we obtain:

$$\langle \Gamma \rangle = F_d a \frac{a}{\lambda} \left[0.644\eta h^2 - 0.58e^2 \right]. \quad (11)$$

This expression vanishes for $e = 1.05\eta^{1/2}h$. However, for $\eta \lesssim 1$, this corresponds to $e \sim h$, beyond the domain of validity of case (i), for which we made the assumption $ea < \lambda$. We therefore now turn to case (ii). In that case, the shear is negligible (Masset & Velasco Romero 2017; Eklund & Masset 2017) and the planet is subjected to the force F_d defined above, directed along its direction of motion with respect to the gas, as long as it remains subsonic. When the velocity with respect to the gas is almost equal to or larger than the sound speed, the thermal force varies as a function of the velocity, and in particular decays sharply in the supersonic regime (Velasco Romero & Masset 2019). The planet's velocity in the frame corotating with the guiding centre is:

$$(\dot{x}, \dot{y}) = ea\Omega_p [\sin(\Omega_p t), 2 \cos(\Omega_p t)] \quad (12)$$

while in that same frame the gas velocity is:

$$(v_x^{\text{gas}}, v_y^{\text{gas}}) = \left[0, -\frac{3}{2}\Omega_p(x + x_p^0) \right] \quad (13)$$

hence the planet's velocity with respect to the gas is:

$$(\dot{x}|_{\text{gas}}, \dot{y}|_{\text{gas}}) = \Omega_p \left[ea \sin(\Omega_p t), \frac{ea}{2} \cos(\Omega_p t) + \frac{3}{2}x_p^0 \right]. \quad (14)$$

From this expression we can infer the components of the unitary vector $\mathbf{n} = (n_x, n_y)$ having same direction as this velocity vector. The thermal force on the planet is then $F_d \mathbf{n}$, and the torque on the planet is:

$$\Gamma = F_d [(a+x)n_y - yn_x]. \quad (15)$$

Upon time averaging, we obtain (see appendix A):

$$\langle \Gamma \rangle = F_d a \left(1.20 \frac{x_p^0}{ea} - 1.54e \right), \quad (16)$$

this expression being valid only for $ea > \lambda$. Again, we see that the average torque decreases as the eccentricity increases. We depict in Fig. 1 the torque as a function of eccentricity, for the two regimes (i) and (ii). As anticipated, the torque remains positive over the domain of validity of regime (i), while it changes sign in regime (ii) for

$$e_{\text{reversal}} = \sqrt{\frac{1.20}{1.54}} \eta h \approx 0.9\eta^{1/2}h \lesssim h. \quad (17)$$

Therefore, if the eccentricity of the planet, driven by the thermal force, saturates to a value in excess of e_{reversal} , migration is inwards, at least if thermal forces dominate over resonant forces. This migration reversal must be put solely on the account of thermal forces. If, in addition, one takes into account the Lindblad and corotation torques, usually negative, the threshold eccentricity is smaller than this value, marginally so for very low mass planets, for which resonant torques are small compared to thermal torques.

The reason for this reversal is depicted in Fig. 2, which shows the heating force at several positions along the epicycle, for a case without a corotation offset. This force has a constant magnitude, and a varying orientation over an orbital period. Its lever arm being larger at apoastron, the torque on the outer part of the epicycle, which is negative, dominates.

This suggests that if the thermal force had a variable magnitude along the epicycle, and a larger value on the inner part, the average torque could remain positive. From Eq. (6), we see that this may happen if the luminosity, the thermal diffusivity or the sound speed vary along the epicycle. For the time being, we remain agnostic of the reasons of the variation, and simply assume that the magnitude

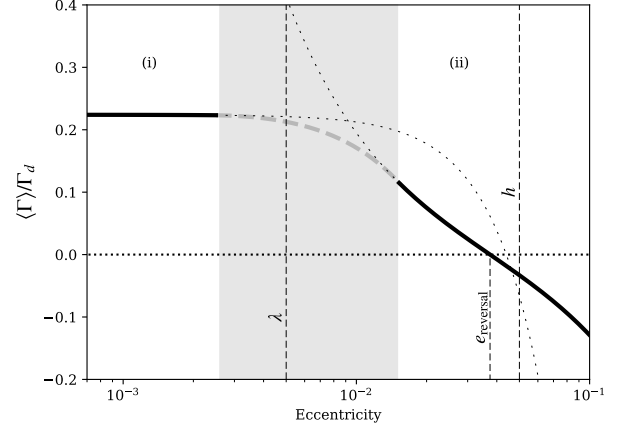


Figure 1. Time averaged torque as a function of eccentricity. The torque is normalised to $\Gamma_d = F_d a$. The thick black solid lines show respectively regime (i) (left) and regime (ii) (right). From left to right, the vertical dashed lines show the thermal lengthscale, the eccentricity at which the torque changes sign and the aspect ratio. For this plot we have assumed $h = 0.05$, $\lambda = 5 \cdot 10^{-3}a$ and $x_p^0 = 1.75 \cdot 10^{-3}a$, corresponding to $\eta = 0.7$. The grey band covers the eccentricity range for which neither regime is valid, the grey dashed line over this interval depicts what the transition between the two regimes may look like, and the thin dotted lines show the extrapolation of the two regimes beyond their domain of validity, using Eqs. (10) and (16). We note that regime (ii) is valid as long as the planet is subsonic, so that for $e > h$ the actual curve would depart from the trend shown here.

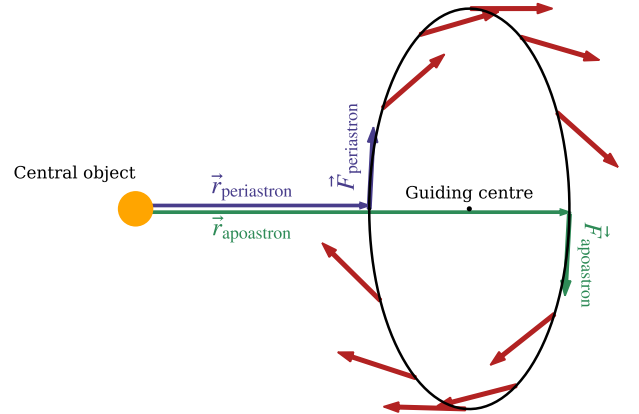


Figure 2. Depiction of the heating force along the epicycle of an eccentric planet. Its magnitude is a constant. In an inertial frame, rotation would be counter-clockwise, hence at periastron the torque of the heating force is positive, and negative at apoastron. The larger lever arm at apoastron entails a larger absolute value for the torque than at periastron.

of the thermal force has a linear dependence on the distance to the central object:

$$F_d(x) = F_d(0) \left(1 + s \frac{x}{a} \right), \quad (18)$$

where s is the dimensionless slope of this dependence. Repeating the calculation of the time average of the thermal force with this new

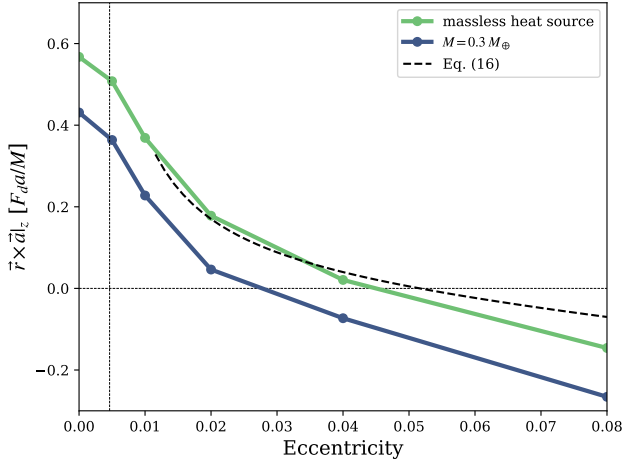


Figure 3. Specific torque as a function of eccentricity for a low-mass planet as described in the text, and thermal torque with same net luminosity for a massless perturber. The vertical dotted line shows the value of λ/a . The dependence expected from Eq. (16) is shown starting at $e = 2.5\lambda/a$. As the specific torque is undetermined for a massless object, we simply compute $\vec{r} \times \vec{a}$, where \vec{a} is the acceleration imparted by the gas disturbance at the location of the planet.

force expression (see Appendix B), we obtain, to first order in e :

$$\langle \Gamma \rangle = F_d a \left[1.20 \frac{x_p^0}{ae} - (1.54 + 0.40s)e \right], \quad (19)$$

where here F_d stands for $F_d(0)$. As anticipated, the torque remains positive for any value of the eccentricity if $s < s_c = -1.54/0.40 \approx -3.85$. For such a value of the slope, the planet experiences a significantly larger thermal force at periastron than at apoastron. Consider a planet with an eccentricity driven to a value comparable to the aspect ratio: $e \sim h \sim 0.05$. The ratio of the force between periastron and apoastron is then $(1 - s_c e)/(1 + s_c e) \sim 1.5$.

As said above, the magnitude of the heating force may vary because the thermal diffusivity, the sound speed or the luminosity of the planet varies. The first two quantities are intrinsic to the disc, and while they might exhibit such large variations over the relatively narrow range $[a(1-e), a(1+e)]$, the luminosity may vary much more, especially in the vicinity of dust rings. Such rings can have widths comparable to or marginally smaller than the pressure lengthscale (Dullemond et al. 2018), so that a planet having an eccentricity comparable to the disc’s aspect ratio and its periastron in the ring will accrete significantly more there than at apoastron. In consequence it should easily fulfil the requirement that the luminosity at periastron be 50% larger than that at apoastron and hence be subjected to a positive thermal torque, on average, provided a sizeable fraction of the potential energy of the accreted material is released as heat into the nearby gas on a timescale much shorter than the orbital timescale. In the following we will use extensive numerical simulations to check this hypothesis and identify the main properties of the dynamics of an accreting low-mass planet in the vicinity of a dusty ring.

Before that, a few final remarks are in order. Pierens (2023) already noticed that it is unlikely that the torque reversal at larger eccentricity can be put on the account of the quenching of the corotation torque (since the reversal also happens when the corotation torque is substantially saturated), and interpret the decrease of the thermal torque with eccentricity as a cut-off. They provide an empirical fit with an

exponential decay as a function of eccentricity (their Eq. 36). From the above we argue that the decrease of the thermal torque is rather a reversal, and that it may masquerade as an exponential cut-off only over a limited range of eccentricity, and only when the planet has a luminosity constant in time. Figure 3 shows the total specific torque exerted on a planet with mass $10^{-6} M_\star$ with a constant luminosity $L = 5L_c$, in a disc with $\Sigma \propto r^{-2}$ (so that the total linear corotation, albeit positive¹, has a very small value: its quenching should have a negligible impact on the net torque). We see that the torque decays and changes sign for $e \lesssim h$ (the large corotation offset of our set of parameters requires a significant eccentricity to revert the torque). The top curve on that figure also shows the specific torque exerted on a vanishingly small mass (so that there is neither resonant nor cold thermal torque) with same net luminosity $5L_c$. That curve is very similar to the previous one, which clearly indicates that the net torque is dominated by the thermal torque, the offset between the two being attributable to the (subdominant) resonant and cold thermal torques. We also see that the thermal torque does not tend toward zero, but changes sign at higher eccentricity, as expected from the calculations above.

The reversal of the time averaged thermal torque is similar to an effect found by Muto et al. (2011) for planets with an eccentricity significantly larger than the aspect ratio. The planet is then subjected to the dynamical friction of the gas, aligned with the relative velocity between the planet and the gas, much as the heating force, but with a negative sign. They find the dynamical friction to scale with the local midplane density of the gas. When the latter is constant (or increases outwards), the average torque is positive (their Fig. 10²).

Our discussion has assumed a thermal torque dominated by heating effects. When the latter are absent, only the “cold finger effect” (Lega et al. 2014) is at play and all our conclusions are reverted: the average torque, negative at small eccentricity, becomes positive above a certain value of the eccentricity. This is of limited interest though, as a finite eccentricity is usually not an equilibrium one for a planet experiencing only the cold and resonant torques. Chrenko & Chametla (2023) find indeed in these circumstances that the average power on the planet is negative, indicating an inward migration. The increase of the area of the orbit, required by the positive torque, is then achieved by lowering its eccentricity (as expected), rather than expanding its semi-major axis.

3 NUMERICAL SIMULATIONS

We make use of FARGO3D (Benítez-Llambay et al. 2019) to perform three-dimensional numerical simulations of low-mass planets embedded in a gaseous protoplanetary disc, accreting dust from a narrow ring, and injecting the energy released by accretion into the nearby gas. The dust is modelled as a pressureless fluid (Benítez-Llambay et al. 2019), and the ring is realised through a prior, two-dimensional simulation in the meridional plane allowing the dust to accumulate near a local pressure maximum in the gas. The accretion method for the dust requires a large resolution near the planet, so we use nested meshes centred on the average radial location of the planet (Velasco Romero & Masset 2019; Velasco Romero et al. 2022).

¹ This linear corotation torque is the sum of three components, related respectively to the vortensity gradient, the temperature gradient and the entropy gradient (Jiménez & Masset 2017).

² That figure shows the timescale for the variations of a , which increases for $\alpha \leq 0$. At the same time e decreases, so that the net torque is positive: both effects indeed add up to increase the area of the orbit.

Owing to the large computational cost of simulating one orbital period, we do not simulate the evolution of a growing planet over a large number of orbits. Rather, we perform many short term simulations that allow us to determine the variation rate of the semi-major and eccentricity as a function of the location and eccentricity of the planet, from which we determine, by interpolation, the orbital evolution of a low-mass planet over large amounts of time.

3.1 Governing equations

The equations that govern the evolution of the gas and dust are the continuity equation, the momentum equation, and an energy equation for the gas.

$$\partial_t \rho_g + \nabla \cdot (\rho_g \mathbf{v}_g) = 0, \quad (20)$$

$$\partial_t (\rho_g \mathbf{v}_g) + \nabla \cdot (\rho_g \mathbf{v}_g \otimes \mathbf{v}_g) = -\nabla P - \nabla \cdot \tau - \rho_g \nabla \Phi, \quad (21)$$

$$\partial_t e_g + \nabla \cdot (e_g \mathbf{v}_g) = -P \nabla \cdot \mathbf{v}_g - \nabla \cdot \mathbf{F}_h + Q, \quad (22)$$

$$\partial_t \rho_d + \nabla \cdot (\rho_d \mathbf{v}_d + \mathbf{j}_d) = 0, \quad (23)$$

$$\partial_t (\rho_d \mathbf{v}_d) + \nabla \cdot (\rho_d \mathbf{v}_d \otimes \mathbf{v}_d) = -\rho_d \nabla \Phi + k(\mathbf{v}_g - \mathbf{v}_d), \quad (24)$$

where $\rho_{g(d)}$ and $\mathbf{v}_{g(d)}$ denote the density and velocity of the gas (dust), τ the viscous stress tensor, e_g and P the density of internal energy and pressure of the gas, Φ the gravitational potential, Q the heat source term arising from the release of accretional energy, \mathbf{F}_h the heat flux arising from thermal diffusion. The expression of the viscous stress tensor has been given elsewhere (e.g. Benítez-Llambay & Masset 2016) and is not repeated here. The kinematic viscosity ν that sets the magnitude of this tensor is evaluated using the α formalism (Shakura & Sunyaev 1973): $\nu = \alpha_\nu \gamma r^2 h^2 \Omega_K$. The pressure is linked to the density of internal energy through:

$$P = (\gamma - 1)e_g, \quad (25)$$

the gravitational potential is given by:

$$\Phi(\mathbf{r}) = -\frac{GM_\star}{r} - \frac{GM}{[|\mathbf{r} - \mathbf{r}_p|^2 + b^2]^{1/2}}, \quad (26)$$

where \mathbf{r}_p is the location of the planet and b the customary softening length of the potential. We do not include in this expression the indirect term arising from the acceleration of the star imparted by the planet because we expect this term to be negligible for the effect considered in this work. The heat source term arising from the accretion luminosity is:

$$Q = L\delta(\mathbf{r} - \mathbf{r}_p), \quad (27)$$

where here only δ stands for Dirac's delta function, while the heat flux is given:

$$\mathbf{F}_h = \chi \rho \nabla \left(\frac{e}{\rho} \right), \quad (28)$$

where the thermal diffusivity χ is given by (e.g. Jiménez & Masset 2017):

$$\chi = \frac{16(\gamma - 1)\sigma T^3}{3\rho^2(\mathcal{R}/\mu)\kappa}, \quad (29)$$

where σ is Stefan's constant, \mathcal{R} the constant of ideal gases, μ the mean molecular weight and κ the opacity, evaluated using the prescription of Bell & Lin (1994). As we consider that the small grains, mainly responsible for the opacity, are well coupled to the gas, we do not take into account the increase of the dust-to-gas ratio in the ring for the evaluation of the opacity, and rely solely on the gas density to evaluate that quantity, using standard well-mixed gas and dust components with a dust-to-gas ratio 0.01. The additional flux \mathbf{j}_d that

features in the equation of continuity on the dust captures the dust diffusion using the method given by Weber et al. (2018):

$$\mathbf{j}_d = -\delta r^2 h^2 \Omega_K (\rho_g + \rho_d) \nabla \left(\frac{\rho_d}{\rho_d + \rho} \right), \quad (30)$$

where δ is a dimensionless coefficient that quantifies the diffusion of dust. In all our calculations, we take $\delta = \alpha_\nu = 10^{-4}$, in line with upper limits of turbulence obtained with ALMA (Flaherty et al. 2020). Finally, the gas-dust friction coefficient k that features in the momentum equation on the dust is:

$$k = \frac{\rho_d \Omega_K}{\tau_s}, \quad (31)$$

where τ_s is the dimensionless stopping time (or Stokes number) of the dust. We note that there is no equivalent term in the momentum equation of the gas: we neglect the feed-back of the dust onto the gas. In all the calculations presented here, we have adopted $\tau_s = 0.01$. This value is rather on the low side of the range of values for which a narrow ring forms. As the Stokes number increases, the width of the ring decreases, enhancing the variation of the accretion rate between periastron and apoastron, while the accretion radius of pebbles increases. It should therefore be kept in mind that the mechanism presented here could be even more efficient if the dust had a Stokes number higher than 0.01.

3.2 Initial conditions

We specify hereafter the different fields of hydrodynamics quantities at $t = 0$, prior to the two-dimensional relaxation run.

$$\rho_g = \frac{\Sigma_0}{\sqrt{2\pi r_0 h}} \left(\frac{r}{r_0} \right)^{-\alpha-1} \sin(\theta)^{-\beta-\alpha-1+\frac{1}{h^2}} \times \left[1 + 4 \exp \left(-\frac{(r-r_0)^2}{2r_0^2 h^2} \right) \right] \quad (32)$$

$$e_g = \frac{\rho_g h^2 G M_\star}{r(\gamma - 1)} \quad (33)$$

$$v_g^\phi = \sqrt{\frac{G M_\star}{r}} \left[1 - (\beta + \alpha + 1) h^2 \right]^{1/2} - \Omega_{\text{frame}} r \sin \theta \quad (34)$$

$$v_d^\phi = \sqrt{\frac{G M_\star}{r}} - \Omega_{\text{frame}} r \sin \theta \quad (35)$$

The dependence of ρ_g on the colatitude θ given in Eq. (32) is that worked out by Masset & Benítez-Llambay (2016) in locally isothermal discs in which the sound speed is a function of the spherical radius. It tends towards the standard Gaussian profile near the mid-plane ($\theta \approx \pi/2$). In Eqs. (32)–(35), r_0 is a reference radius close to the ring maximum, Σ_0 would be the disc's surface density at r_0 in the absence of the “bump” imposed by the last factor of Eq. (32), h is the aspect ratio of the gaseous disc (assumed constant), α is the “slope” of surface density ($\alpha = -d \log \Sigma / d \log r$) and β that of temperature ($\beta = -d \log T / d \log r$). We choose $h = 0.05$, $\Sigma_0 = 10^{-3} M_\star / r_0^2$, $\alpha = 1/2$, and have $\beta = 1$ as per our assumption of a constant aspect ratio. We specify to the case $r_0 = 10$ au and M_\star is a solar mass. The value of the surface density then amounts to 1.65 times that of the MMSN at 10 au. The slope of surface density corresponds to a shallow decay routinely used in simulations with smooth discs. We anticipate that our results are hardly impacted, if at all, by this value, as most of the effect we present here arises from dominant thermal forces in the ring, and since the variation of the surface density over the radial excursion of the planet is small.

The initialisation of the dust density is done in a way that handles poorly resolved layers in the vertical direction. Indeed, when the disc is resolved over a very small number of zones in the vertical direction, sampling the density using the standard Gaussian expression evaluated at the zone centres does not guarantee that a vertical integration yields the desired surface density. Rather, we evaluate the density as the (discrete) derivative of an error function, which by construction allows to enforce the value of the integral of that quantity (i.e., the surface density). When the resolution is sufficient, the result is indistinguishable from the direct evaluation of a Gaussian profile:

$$\rho_d = \Sigma_0 Z \left(\frac{r}{r_0} \right)^{-\alpha} \left[\operatorname{erf} \left(\frac{\pi/2 - \theta_-}{\sqrt{2}h_d} \right) - \operatorname{erf} \left(\frac{\pi/2 - \theta_+}{\sqrt{2}h_d} \right) \right] \frac{1}{2r\Delta\theta}, \quad (36)$$

where Z is the dust-to-gas ratio, $h_d = \sqrt{\delta/(\tau_s + \delta)}h$ (Youdin & Lithwick 2007) is the aspect ratio of the dusty disc, θ_- (θ_+) is the lower (upper) bound of a zone in colatitude, and $\Delta\theta \equiv \theta_+ - \theta_-$. Regardless of the value of $h_d/\Delta\theta$, the formulation of Eq. (36) always yields a column density of dust $Z\Sigma_0(r/r_0)^{-\alpha}$. While the dust layer is correctly resolved on the patch of highest resolution, this may not be true on the base mesh, and this treatment avoids to have discontinuities of the column density of dust across mesh boundaries. In all simulations presented here we have $Z = 0.01$.

3.3 Meshes and setup

The disc is described on a set of four nested, spherical meshes. The azimuthal extent of the base mesh is 1.6 rad, largely smaller than 2π , to save computational time. The frame corotates with the planet, so that its angular frame oscillates in time when the planet is eccentric. This entails that the planet's trajectory is a radial segment, and allows to restrict the azimuthal extent of the refined patches. The extent of the different levels is specified in Tab. 1.

3.4 Relaxation of initial conditions: creation of the dusty ring

The initial conditions outlined in section 3.2 do not correspond to a disc in rotational equilibrium: among other things, the bump introduced in the density (and therefore pressure) is not reflected in the azimuthal speed. Besides, the dust density is simply a scaled version of that of the gas: the dust has not yet accumulated in the vicinity of the pressure maximum, so that there is no thin dusty ring in the initial conditions. For these reasons, we perform a two-dimensional calculation in the (r, θ) plane in order to allow the disc to relax toward rotational equilibrium, and to allow the dust ring to form. This initial relaxation is performed only on the base mesh ($\ell = 0$, see Tab. 1), with only one zone in azimuth.

We find that 270 orbital periods at r_0 are enough to obtain profiles that do not vary significantly in time and allow us to measure the effect of the dust ring on an eccentric planet. The initial bump of gas density and pressure widens significantly, and its amplitude decays, but a local maximum of pressure remains, which allows the dust to converge and form a thin ring. We show the converged profiles in Fig. 4. A Gaussian fit near the pressure maximum upon relaxation yields a width of the pressure bump $w_g = 2.5r_0h$ and a relative amplitude ~ 2 , which indicates that it should not be subjected to the Rossby Wave Instability (RWI) and that the dust trap should survive (Chang et al. 2023, their Fig. 2). The mass of the dust ring obtained after relaxation is $10 M_\oplus$. From the width of the pressure bump, one can estimate the expected width of the dust ring (Dullemond et al. 2018):

$$w_d = w_g \sqrt{\alpha_v/\tau_s}. \quad (37)$$

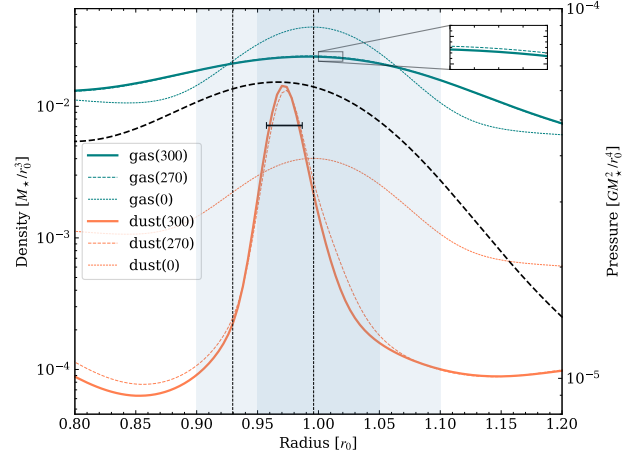


Figure 4. Midplane densities (solid lines) and pressure (dashed line) after 300 orbits. The thin dotted lines show the initial profiles of gas and dust densities, while the thicker dotted lines show these profiles after 270 orbits. The scale of pressure (right vertical axis) is chosen so as to show that the thin dust ring has its peak density at the pressure maximum. The horizontal segment on the peak of dust density shows the FWHM expected for the dust ring. The radial domain covers what would be the radial extent of the mesh at level $\ell = 1$ (for a planet with $a = 1$), while the light vertical bands show the extent of levels $\ell = 2$ and $\ell = 3$. These bands are shown for informational purpose only, as nested meshes are not used during the relaxation run. For future reference, the vertical dashed lines show the location of the two migration traps of a cold, low mass planet on a circular orbit, subjected to the gas and dust torques, discussed later in the text.

The corresponding FWHM is shown on Fig. 4 and matches satisfactorily the width of the dust ring. While, as stated above, the pressure bump is not expected to experience the RWI, it could still be subjected to a more complex version of that instability involving dust (DRWI, Liu & Bai 2023), in particular that involving a mild pressure bump. Since we do not take into account the dust feedback onto the gas, this instability should not happen in our setup. Furthermore, the short timescale over which our three-dimensional runs are performed would preclude the appearance of this instability.

3.5 Restart as a three-dimensional run

Once the ring of dust has formed and the disc profiles have converged to profiles constant in time, we extend the domain for ϕ over the range $[-.8, .8]$ with $N_\phi = 400$ (hence $\Delta\phi = 4 \times 10^{-3}$). We also include three levels of refinement in order to reach $\Delta_{r,\phi,\theta} = 5 \times 10^{-4}$, using the patches detailed in Tab. 1. We insert a low-mass planet on a non-inclined, eccentric orbit, using a sinusoidal taper over a timescale that corresponds to one orbital period at r_0 :

$$M(t) = \begin{cases} M \sin^2 \left(\frac{\Omega_0 t}{4} \right) & \text{if } t < 2\pi/\Omega_0 \\ M & \text{otherwise,} \end{cases} \quad (38)$$

where $\Omega_0 = (GM_\star/r_0^3)^{1/2}$ is the Keplerian frequency at r_0 . This tapering is immaterial for the problem at hand: the timescale of the disc's response is significantly shorter than the orbital period (Masset & Velasco Romero 2017; Eklund & Masset 2017), hence the variation rates of the semi-major axis and eccentricity, measured over the last orbital period, are virtually independent of the mass growth imposed over the first orbit. The planet accretes dust from the disc and releases

the energy obtained from accretion into the ambient gas. We detail the implementation of these two processes below.

3.6 Dust accretion

We model the accretion of dust by removing a fraction of the material in the cells nearest to the planet. Our rationale for using this procedure is that the size of the cells on the layer of highest resolution is significantly smaller than the accretion radius within which pebbles are in the settling regime, even for the smallest planetary mass considered in this study. Furthermore, the settling time at the distance from the planet comparable to the resolution is shorter than or comparable to the timestep arising from the Courant condition. For the cells (i, j, k) that comply with $|\phi_p - \phi_{ijk}| < \Delta\phi$, $|r_p - r_{ijk}| < \Delta r$ and $|\theta_p - \theta_{ijk}| < \Delta\theta$, i.e. the cells nearest to the planet, the dust is removed using the following recipe. We evaluate:

$$\Delta\rho_{ijk} = \rho_{ijk} \left(1 - \frac{\phi'_{ijk}}{\Delta\phi}\right) \left(1 - \frac{r'_{ijk}}{\Delta r}\right) \left(1 - \frac{\theta'_{ijk}}{\Delta\theta}\right), \quad (39)$$

where $\xi'_{ijk} = |\xi_p - \xi_{ijk}|$ for $\xi \equiv \phi, r, \theta$.

The new dust density is then:

$$\rho'_{ijk} = \rho_{ijk} - \Delta\rho_{ijk} \quad (40)$$

and the accretion rate is simply:

$$\dot{M} = \sum_{ijk} \frac{\Delta\rho_{ijk} V_{ijk}}{\Delta t}, \quad (41)$$

where V_{ijk} is the volume of the cell (i, j, k) and the sum is performed over the cells for which the density was changed.

In order to validate this approach, we have compared the accretion rates obtained with this procedure to those obtained semi-analytically by evaluating the accretion radius as a function of the relative velocity between the planet and the pebbles. We find a reasonable agreement between the two, generally within a factor of two. As we shall see in section 4.3, we find that the accretion efficiency depends on the planet's luminosity. Should we had forced the simulations to use an accretion rate based on formulae that ignore the planet's luminosity, we would have missed this side result.

The accreted mass of the pebbles is not added to that of the planet. Likewise, the momentum accreted is not added to the planet. We shall discuss this in section 5.5.4.

3.7 Heating

The accretion rate \dot{M} is then used to compute the luminosity of the planet:

$$L = \frac{GM\dot{M}}{R_p}, \quad (42)$$

where $R_p = \left(\frac{3M}{4\pi\rho_p}\right)^{1/3}$ is the planet's physical radius. In this expression we adopt for the density of the planet $\rho_p = 3 \text{ g cm}^{-3}$. Note that in Eq. (42) we use M , the mass at the end of the short, progressive growth (see section 3.5) and the corresponding physical radius R_p , rather than $M(t)$ and a corresponding instantaneous radius $R_p(t)$. The luminosity is therefore overestimated over the initial mass ramp. However, this initial growth stage is entirely artificial and has no impact on the variation of the orbital elements measured on the last orbit, owing to the short response time of the thermal force.

The luminosity is then used to increase the density of internal

energy of the gas in the neighbouring cells, i.e. those which fulfil the same distance criteria as those used for the accretion of dust (see section 3.6):

$$\Delta e_{ijk} = L \left(1 - \frac{\phi'_{ijk}}{\Delta\phi}\right) \left(1 - \frac{r'_{ijk}}{\Delta r}\right) \left(1 - \frac{\theta'_{ijk}}{\Delta\theta}\right) \frac{\Delta t}{V_{ijk}}. \quad (43)$$

This method is the same as that used by Eklund & Masset (2017).

A more sophisticated prescription for the injection of heat into the nearby gas has been investigated by Velasco Romero & Masset (2020), and found to essentially yield same results as the simpler prescription considered here. The reason for that is that the asymmetry of the heated region, which induces the thermal force, kicks in at distances from the planet larger than the release radius.

4 RESULTS

We present hereafter the results of our numerical simulations. We firstly present in detail our fiducial calculation, that of a one-Earth mass protoplanet orbiting in the vicinity of the ring obtained at section 3.4, before presenting additional results for other masses and/or a slightly modified setup.

4.1 Fiducial calculation

Our fiducial calculation consists of a systematic exploration of the semi-major axis, eccentricity space for a one Earth-mass planet. The set of semi-major axis values is $\{0.82r_0 + 0.02r_0i \text{ for } i \in [0, 13]\} \cup \{0.97r_0\} \cup \{1.12r_0\}$ (16 values in total), while the set of eccentricity values is $\{1.25 \cdot 10^{-3} \times 2^i \text{ for } i \in [0, 3]\} \cup \{0.02i \text{ for } i \in [1, 6]\}$ (10 values in total). The total number of runs of this fiducial exploration is therefore 160. Each run lasts three orbital periods at r_0 . The planet is free to move under the disc's force, which we evaluate by subtracting the azimuthal average of the density from each given cell prior to evaluating the force it exerts on the planet. This method has been suggested as a workaround for the spurious shift of resonances that occurs when the disc's self-gravity is discarded (Baruteau & Masset 2008; Benítez-Llambay et al. 2016; Ataiee & Kley 2020). While this effect would at best be minute here, it is also important to use this method when working on a wedge of the disc, as we do here: if the planet does not lie exactly on the bisector line of the wedge, it would be subjected to a strong, spurious force arising from the asymmetry of the mass distribution around it, even if the disc is unperturbed. We measure the drift of its semi-major axis and eccentricity over the last planetary orbit. Namely, if t_f is the last time at which we get a measure of a and e in the log files, we seek the value of a and e at $t_i = t_f - 2\pi\sqrt{a^3/GM_\star}$. Except for $a = r_0$, this time is in general not found in the log files (owing to our uniform time sampling across all runs) and the corresponding value of a and e is obtained by linear interpolation. The time derivatives of a and e are then approximated as:

$$\dot{a} \approx \frac{a(t_f) - a(t_i)}{t_f - t_i} \quad \text{and} \quad \dot{e} \approx \frac{e(t_f) - e(t_i)}{t_f - t_i}. \quad (44)$$

We show in Fig. 5 a map of the time derivative of eccentricity and semi-major axis as function of these two quantities. These maps show that

- the eccentricity is excited up to values slightly larger than the disc's aspect ratio for planets whose orbit cross the ring. When the orbit does not cross the ring, the eccentricity is damped (for planets

ℓ	(N_ϕ, N_r, N_θ)	$(\phi_{\min}, \phi_{\max})$	(r_{\min}, r_{\max})	$(\theta_{\min}, \theta_{\max})$
0	(400, 200, 30)	$[-.8, .8]$	$a + [-0.4, 0.4]r_0$	$[\frac{\pi}{2} - .12, \frac{\pi}{2}]$
1	(200, 200, 60)	$[-.2, .2]$	$a + [-0.2, 0.2]r_0$	$[\frac{\pi}{2} - .12, \frac{\pi}{2}]$
2	(200, 200, 60)	$[-.1, .1]$	$a + [-0.1, 0.1]r_0$	$[\frac{\pi}{2} - .06, \frac{\pi}{2}]$
3	(200, 200, 60)	$[-.05, .05]$	$a + [-.05, .05]r_0$	$[\frac{\pi}{2} - .03, \frac{\pi}{2}]$

Table 1. Size and extent of each level of the system of nested meshes. The central radius of each level corresponds to the semi-major axis of the planet.

inside the ring) or driven to moderate values (for planets on the outside);

- the semi-major axis of planets that have their periastron in the ring tends to increase with time, whereas it decreases with time for planets that have their apoastron in the ring.

We identify the contours where the eccentricity or the semi-major axis remain constant. Their intersection correspond to orbits that do not evolve in time: they have $\dot{e} = 0$ and $\dot{a} = 0$. These orbits are not necessarily stable. Consider for instance the point near $a = 0.98r_0$ and $e = 0.073$, represented by a cross. This point is obviously unstable as a planet displaced to the right (left), will experience an increase (decrease) of its semi-major axis.

There are two other points, however, identified by a magenta disc on the right plot of Fig. 5, that may correspond to stable orbits. We study the trajectories in the (a, e) plane to assess this stability, using the interpolated maps of \dot{e} and \dot{a} . The results are shown in Fig. 6, which confirms that these two points do indeed correspond to stable orbits. Depending on its starting location in the (a, e) plane, a planet will end up at one of these two points, over a timescale of order $10^3 - 10^4$ years. We evaluate the accretion rate at these fixed points. It is calculated in the same manner as \dot{e} and \dot{a} : we evaluate it over the last orbit, and we interpolate it at the location of the fixed points. We plot the map of $\dot{M}(a, e)$ in Fig. 7, and show the location of the two fixed points. At the outer fixed point, we measure $M/\dot{M} \approx 22 \cdot 10^3 \Omega_p^{-1}$ or $1.1 \cdot 10^5$ yrs, while at the inner fixed point we measure: $M/\dot{M} \approx 58 \cdot 10^3 \Omega_p^{-1}$ or $2.9 \cdot 10^5$ yrs.

4.2 Interpretation of the results

Our results are compatible with the action of a strong thermal force that arises every time the planet goes into the ring. They can be recast in terms of the time derivative of the periastron and apoastron distances, which are respectively:

$$r_- = a(1 - e) \quad \text{and} \quad r_+ = a(1 + e). \quad (45)$$

We see in Fig. 8 that planets that have their periastron in the ring experience a strong increase of their apoastron, and nearly no variation of the periastron. Such planets are subjected to a strong thermal force as they pass through periastron (see left sketch of Fig. 9). The net effect of this passage is an increase of their orbital velocity at periastron. This entails that the periastron distance is conserved, while their apoastron is increased by some amount Δr_+ (and their semi-major axis by $\Delta r_+/2$). Reciprocally, a planet that has its apoastron in the ring is subjected to a strong, resistive thermal force during its passage through apoastron (see right plot of Fig. 8 and right sketch of Fig. 9), resulting in a decay of the periastron distance (and of the semi-major axis by half that of the periastron).

A planet with initially a semi-major axis larger than the ring's radius will park itself at a semi-major axis and eccentricity such that it accretes from the ring at periastron, and such that the kicks of energy and angular momentum it receives there from the thermal force make up for the decay of these quantities over the rest of their epicycle. This corresponds to the outer fixed point. This implies that

the trapping at the outer fixed point relies only on the existence of the narrow dusty ring, not on the existence of the pressure bump: the planet always remain in a region where the pressure decreases monotonically outwards. Should a ring exist in the absence of a pressure bump, we would expect a similar effect to operate.

The inner fixed point corresponds to an effect somewhat similar to the case studied in section 2: above a critical eccentricity that is a fraction of the aspect ratio, migration reverses from outward to inward, and at the critical eccentricity for reversal, migration stops. Too far from the ring, the accretion luminosity is not sufficient to maintain a finite eccentricity and the latter decays, while too close to the ring, the eccentricity is driven to values higher than the critical value for migration reversal. In between these two cases, there is a distance to the ring such that the eccentricity is driven precisely to the value for which migration stalls, which corresponds to the inner fixed point.

4.3 Variation from the fiducial calculation: efficiency of accretion

We now deviate from our fiducial setup and repeat our calculations with a different luminosity of the planetary cores. Namely, instead of Eq. (42), the luminosity is now given by:

$$L = \varepsilon \frac{GM\dot{M}}{R_p}, \quad (46)$$

where $\varepsilon \in [0, 1]$ is a reduction factor that accounts for the fact that the pebbles accreted do not impinge on the surface of the core and are instead vaporised before reaching the surface, contributing to the formation of a high metallicity envelope (Brouwers et al. 2018). While the mass accretion rate keeps same value as before, the energy released in this case is smaller than the value given by Eq. (42), which can be regarded as a maximum value. We have considered $\varepsilon = 0.25$ and $\varepsilon = 0.1$. For the sake of brevity, we do not reproduce here the corresponding maps of \dot{e} and \dot{a} , and directly show the trajectories in the (a, e) plane in Fig. 10 and the map of mass accretion rate in Fig. 11. We find that the two fixed points identified in our fiducial exploration subsist, with similar characteristics (one outside the ring and one inside, the outside one having a larger eccentricity). As the reduction factor ε of the luminosity decreases, these points move toward the ring and their eccentricity decreases. We see in Fig. 11 that for a smaller reduction factor, the fixed points have a location with higher accretion rate. Namely, we find that for a 25% reduction factor, both fixed points correspond to a very similar accretion rate with mass doubling time $M/\dot{M} = 13.6 \cdot 10^4 \Omega_p^{-1}$ or 69 kyr for a central object with a solar mass, significantly smaller than the mass doubling time of the fiducial calculation. This trend to a smaller mass doubling time continues for a 10% reduction factor, with a doubling time for a planet at the inner fixed point of $10^4 \Omega_p^{-1}$ orbits or 50 kyr, and $8.8 \cdot 10^4 \Omega_p^{-1}$ or 44 kyr at the outer fixed point.

Examination of Figs. 7 and 11 shows that the mass accretion rate, for a given value of a and e , depends on ε : the smaller this value, the larger the accretion rate. The radiative feedback from the planet onto

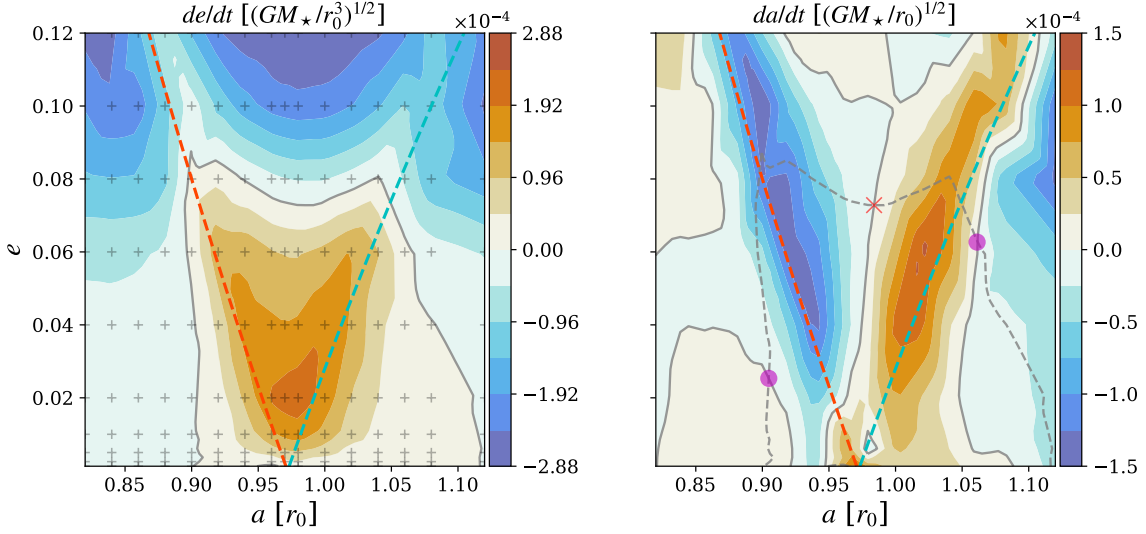


Figure 5. Time derivative of eccentricity (left) and semi-major axis (right) as a function of semi-major axis and eccentricity, for our fiducial exploration. The red (blue) inclined dashed line corresponds to planets that have their apostron (periastron) at the maximum of the dust ring. Planets between these two lines cross the ring maximum. The crosses on the left plot correspond to the values used in our runs. The results are interpolated, upon triangulation, to produce the maps. For legibility reasons, the same crosses have not been reproduced on the right plot. The dashed grey contour of the right plot is a copy of the contour $\dot{e} = 0$ from the left plot. Its intersection with the solid grey contours corresponding to $\dot{a} = 0$ yields locations where the orbit has constant semi-major axis and eccentricity. Magenta filled circles denote stable equilibrium points while the cross identifies an unstable equilibrium (see text for details).

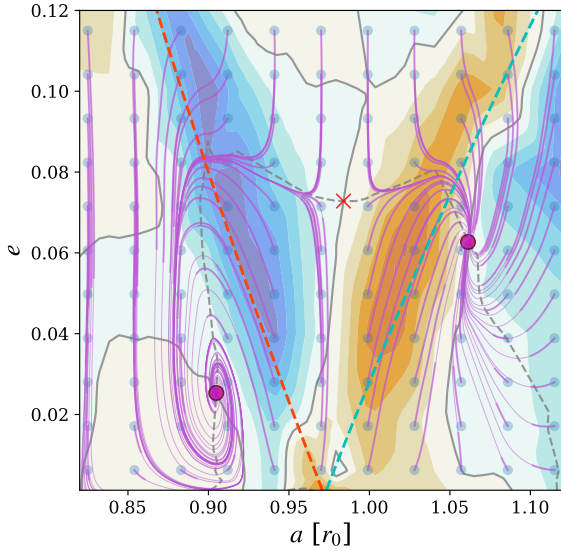


Figure 6. Trajectories in the (a, e) plane for our fiducial exploration, superposed on the map of \dot{a} . The 11×11 blue dots are the starting points. Each trajectory is represented by a thicker line for an integration time up to $500\sqrt{r_0^3/GM_\star}$, i.e. ≈ 80 orbital periods at r_0 , or ≈ 2500 yrs if the central object has a solar mass.

its immediate vicinity tends to evacuate the gas to larger distances. By doing so, it also lowers the dust content that the planet can accrete.

4.4 Effect at other planetary masses

We have investigated how the mechanism operates for planetary masses different from the fiducial mass. Fig. 12 shows an example of

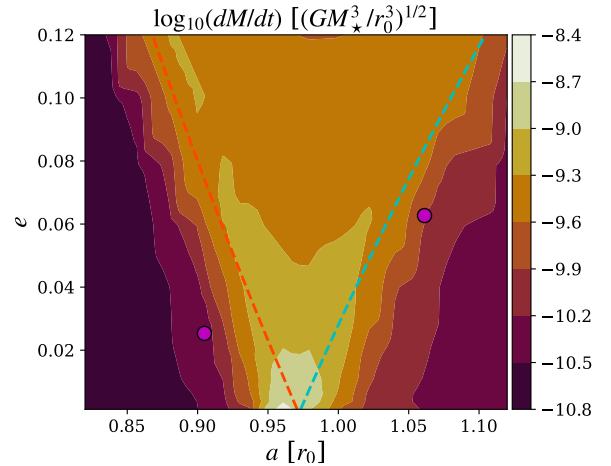


Figure 7. Orbital averaged mass accretion rate in our fiducial runs, as a function of semi-major axis and eccentricity. The two fixed points identified in Fig. 5 are marked as magenta discs.

the gas and dust response at the disc midplane soon after the passage at periastron of a $4 M_\oplus$ planet, while Fig. 13 shows the response after the passage at periastron of an $8 M_\oplus$ planet, both within the midplane and vertically. We identified the fixed points in a number of cases. In order to limit the computational cost, we only explore small patches of the (a, e) plane where we expect to find the fixed points (and we extend these patches in case it is necessary). We then measure the mass accretion rate at each fixed point identified. Tab. 2 summarises the different numerical explorations that we have undertaken.

We show in Fig. 14 and 15 the positions of the right and left fixed points, respectively.

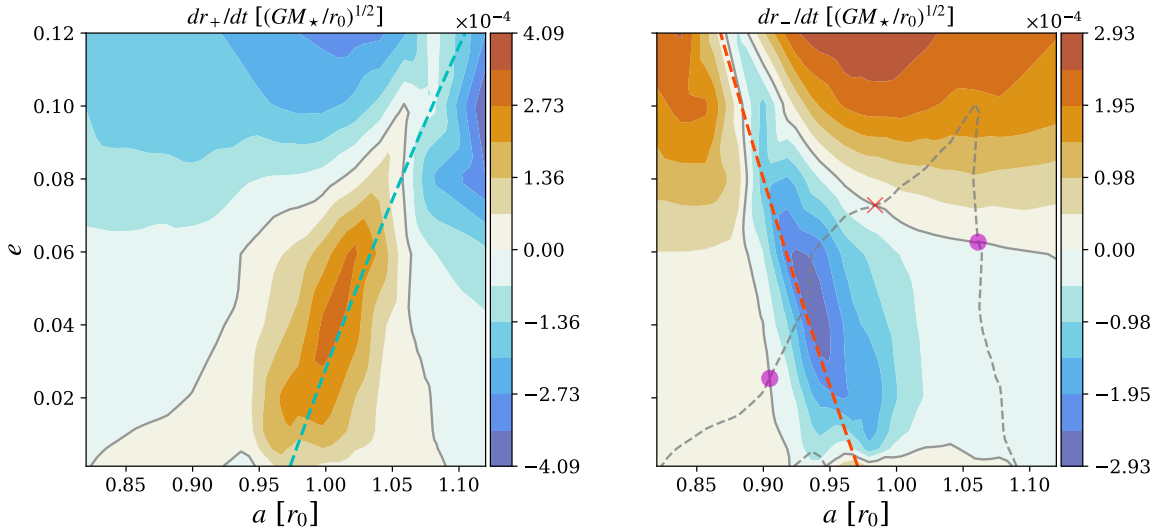


Figure 8. Time derivative of the apoastron (left) and of the periastron (right). For an eccentricity smaller or of the order of the aspect ratio, the main effect of the interaction with the ring is an increase of the apoastron for planets that have their periastron in the ring (those on the blue dashed line of the left plot) and a decrease of the periastron for planets that have their apoastron in the ring (those on the red dashed line of the right plot). Blue contours correspond to the value zero. The dashed grey contour of the right plot is a copy of the contour $\dot{r}_+ = 0$ of the left plot. We recover the two fixed points corresponding to $\dot{a} = 0$ and $\dot{e} = 0$.

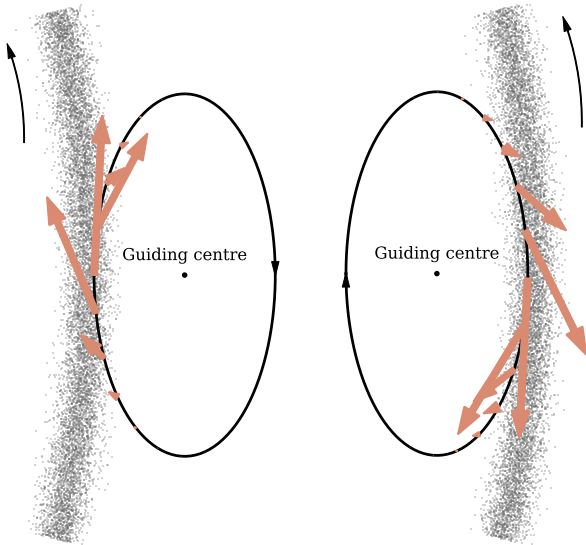


Figure 9. Sketch of a planet that has its periastron in the ring (left) or its apoastron in the ring (right). The rotation of the ring in an inertial frame is counterclockwise, as indicated by the arrow near the top of the plots. In the frame corotating with the guiding centre, the epicycle is described in the clockwise direction. The left (right) plot corresponds to a planet on the blue (red) dashed line of the left (right) plot of Fig. 8

The outer fixed points, independently of ε , show a trend to move to larger semi-major axis and higher eccentricity as the planet's mass increases. For a planetary mass of order $\sim 4 M_{\oplus}$, this trend reverses and the semi-major axis decreases, while the eccentricity can also decrease. We also see that the periastron distance tends to move

Table 2. Summary of the numerical explorations presented in this work. A letter W indicates that a wide exploration of the (a, e) parameter space has been performed (as presented in section 4.1). A letter L (R) stands for a set of calculations that surround the left (right) fixed point. The case W_f corresponds to the fiducial exploration.

M	$0.1 M_{\oplus}$	$1 M_{\oplus}$	$2 M_{\oplus}$	$4 M_{\oplus}$	$8 M_{\oplus}$
$\varepsilon = 0.1$	–	W	LR	LR	R
$\varepsilon = 0.25$	LR	W	LR	LR	R
$\varepsilon = 1$	LR	W_f	–	R	R

toward the centre of the dust's ring as the mass increases, although this trend is not systematic. In two cases, the planets of largest mass ($8 M_{\oplus}$) cross the ring centre.

The inner fixed point show similar trends with opposite sign for the variation of the semi-major axis, except for the case $\varepsilon = 1$, for which we only have two points. The results that we have seen in section 4.3 generalise to all masses: the inner fixed point has smaller eccentricity than the outer fixed point, and the distance of closest approach to the ring is also larger for the inner point.

Fig. 16 shows the mass doubling times obtained for the different fixed points studied in the present work. A fit of these times is subsequently used to provide the planetary mass as a function of time for different values of ε , at the inner and outer fixed points, up to the largest mass considered in our study ($8 M_{\oplus}$), which we can consider representative of the critical mass for runaway gas accretion. Since the mass doubling times have been obtained for a ring with $10 M_{\oplus}$ of dust, the time evolution of the planetary mass is representative of the case in which the ring is permanently replenished by inwardly drifting dust so as to keep its mass at $10 M_{\oplus}$. We recover the fact that the mass grows faster for a smaller value of ε , and that a trapping at the outer orbit favours a faster growth. For the least favourable case, that of a planet trapped on an inner orbit with $\varepsilon = 1$, it takes almost 2 Myr for the planet to reach $8 M_{\oplus}$, while in the most favourable

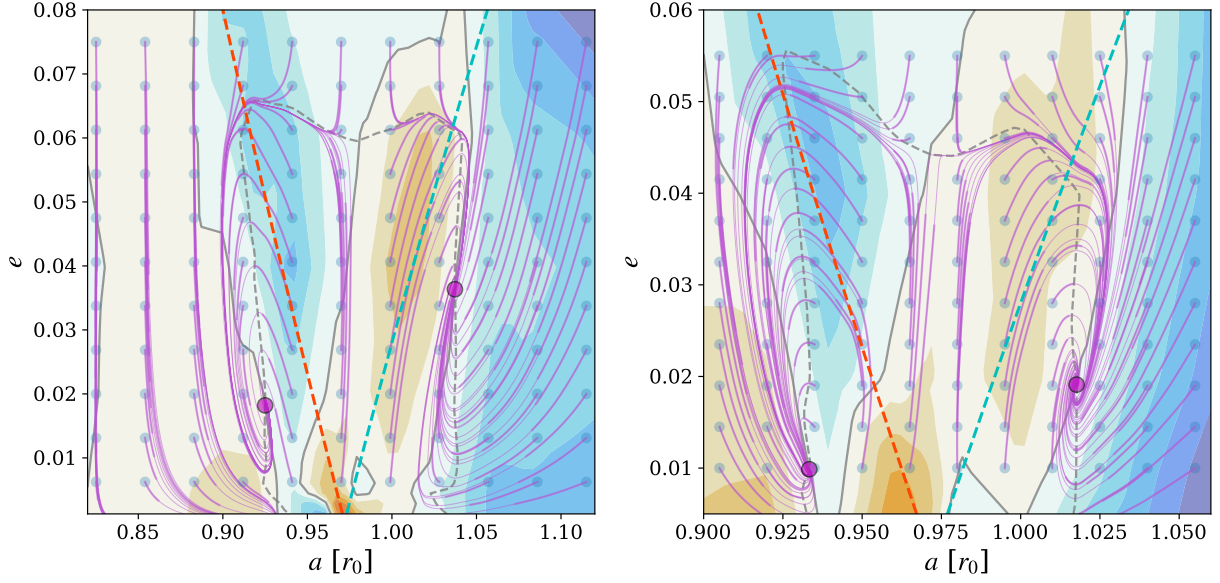


Figure 10. Same as Fig. 6, except for a reduction factor of the luminosity of 25% (left) and 10% (right). Note that the axes limits are different on these two plots.

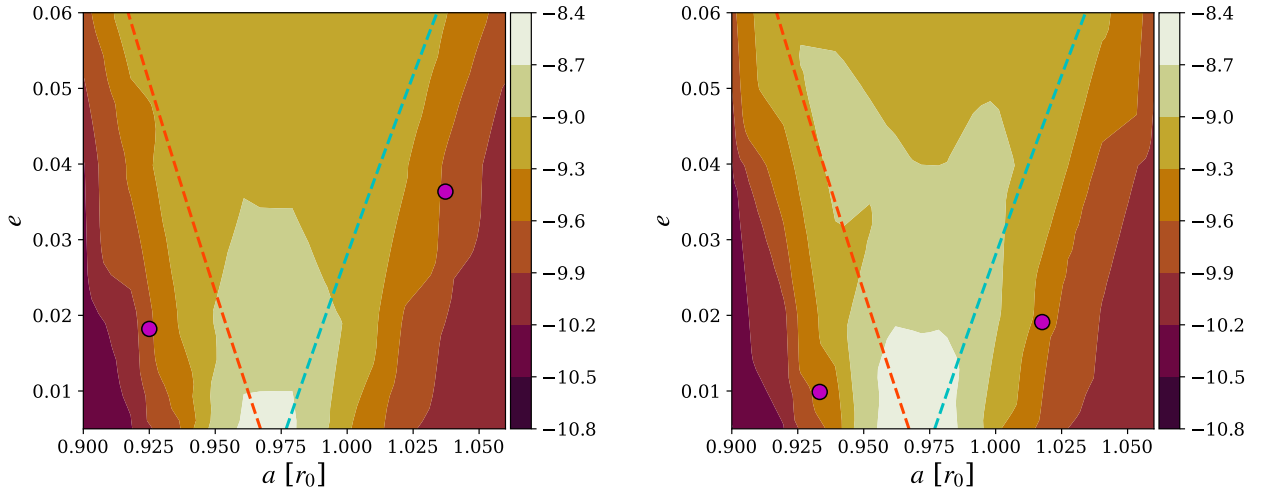


Figure 11. Same as , Fig. 7 except for a reduction factor of the luminosity of 25% (left) and 10% (right). Note that the limits of the left plot have been adjusted to match those of the right plot.

case, that of a planet trapped on an outer orbit with $\varepsilon = 0.25$, this growth is completed in only 200 kyr.

5 DISCUSSION

5.1 Growth inside or outside the ring: a possible dichotomy

We have found that protoplanets in the vicinity of a dusty ring can be trapped either on an inner eccentric orbit or an outer eccentric orbit. We have also found that in general, an outer eccentric orbit goes deeper into the ring (at periastron) than does an inner eccentric orbit (at apoastron), with the consequence that the mass growth is significantly slower for a planet trapped on an inner eccentric orbit. The ultimate fate of a very low mass core forming in the ring therefore depends strongly on which of the two fixed points in (a, e) space it

will eventually reach. If it goes to the outer fixed point, it may reach the critical mass for runaway gas accretion in a few 10^2 kyr (for our disc parameters and a ring at 10 au), whereas it may remain a super-Earth if it goes to the inner fixed point. We have performed additional calculations of a non-luminous Mars-sized embryo on a circular orbit at different orbital radii in the ring. We have seen in the previous sections that even a Mars-sized embryo would have its eccentricity excited by the feedback of its accretional luminosity. Setting here the luminosity to zero gives therefore an indication of how the torque depends on the orbital radius for an even lower mass planet, with a subcritical luminosity, which is still on a circular orbit. We see in Fig. 17 that the total torque cancels out at several radial locations. When the radial derivative of the torque is negative, such a location constitutes a trap (whereas if the derivative is positive, the location is unstable, as can be easily checked). The two trap

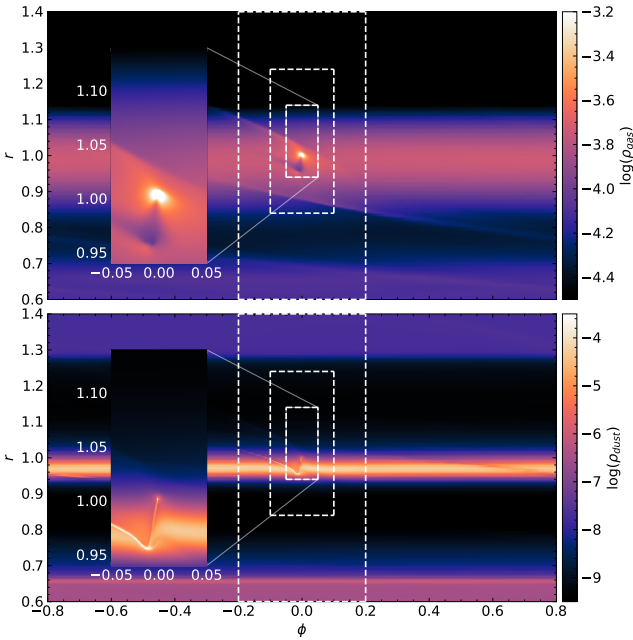


Figure 12. Midplane gas density (top) and dust density (bottom) after the passage at periastron of a $4 M_{\oplus}$ planet with eccentricity 0.064, semi-major axis $1.04r_0$ and accretion efficiency $\varepsilon = 0.25$. The planet’s orbital phase is 0.15 (it would be 0 at periastron and 0.5 at apoastron). It is en route to larger radii and leaves in the gas a hot, under dense trail, clearly visible on the close up of the top plot. The planet in this setup has an orbit close to the fixed point (second larger green dot in Fig. 14). Its radial excursion is marginally smaller than the extent of the layer of highest resolution, from $0.973r_0$ to $1.107r_0$. There is a hint of perturbations in the dust away from the planet, at azimuth $|\phi| \sim 0.6 - 0.7$.

locations are found here near $r = 0.93r_0$ and $r = r_0$, and the torque at the pressure maximum is positive, which suggests that an embryo born at the middle of the ring will eventually get trapped near r_0 . As the planet mass grows, it becomes luminous. Initially it has a subcritical luminosity ($L < L_c$) and thus remains on a circular orbit. As the luminosity grows, the gas torque is no longer dominated by the cold thermal torque (Lega et al. 2014), and at the point at which the luminosity becomes critical and eccentricity starts growing, the heating and cold thermal forces cancel each other, so that the torque has nearly its adiabatic value (Masset 2017). We also plot in Fig. 17 the total torque when the gas is adiabatic. It still shows a trap near r_0 , which suggests that as the embryo will start growing its eccentricity, it will eventually reach the outer fixed point. Nonetheless, owing to the complexity of the torque behaviour with radius, it sounds plausible that, depending on the circumstances, a planet could also reach the inner point. Pierens & Raymond (2024) find that a planet growing near the dust peak eventually migrates inwards or outwards, depending on whether they include the feedback of the dust onto the gas (and they find, with feedback, the result that we find here without feedback). This underlines the extreme sensitivity of the path of the planet to the details of the physical processes responsible for the torque, and suggests that a bifurcation can occur when the planet starts becoming eccentric, with considerable consequences on its destiny. Assessing which of the two fixed points a growing embryo will eventually reach in a general case warrants significant further work.

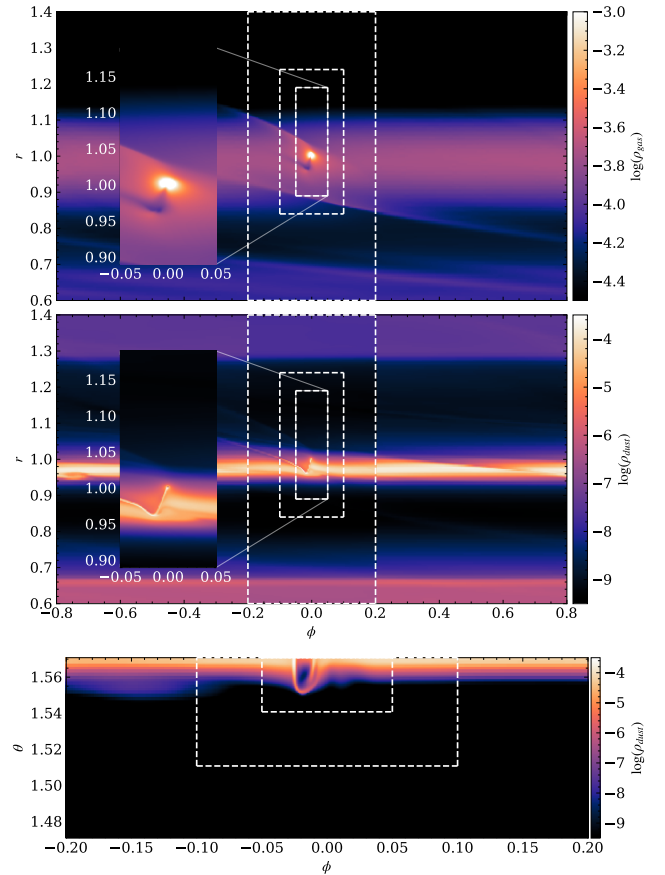


Figure 13. Same as Fig. 12, but for an $8 M_{\oplus}$ planet with eccentricity 0.06, at orbital phase 0.14. The other parameters are the same. The perturbation in the dust ring away from the planet is more apparent. It is due to a previous incursion of the planet. The bottom plot shows a cut of the dust density at $r = r_{\text{ring}} = 0.97r_0$. We see that the dust response is complex and markedly different from that of the gas. It shows an accumulation on a sheet in the region of low gas density, and a lift off the midplane.

5.2 Frequency mismatch between the planet and the ring: consequences

Every time the eccentric planet makes an incursion in the ring, it accretes dust and leaves a “scar” on the ring, with a typical width equal to the radius r_{acc} of pebble accretion. At the next passage, owing to the frequency mismatch between its orbital frequency and the orbital frequency in the ring at the radius of the planet’s incursion, the planet accretes from another, unperturbed region of the ring. The time it takes for the first perturbation to coincide again with the planet is equal to the synodic period of the ring seen by the planet, and is of order of:

$$T_{\text{syn}} \sim \frac{2\pi}{|r\partial_r\Omega|e} = \frac{4\pi}{3e}\Omega^{-1} \quad (47)$$

This value is to be compared with the time it takes to erase the scar by dust diffusion. We make hereafter a conservative derivation of this time, in which we neglect the Keplerian shear.

$$T_{\text{diff}} = \frac{r_{\text{acc}}^2}{\delta c_s^2/\Omega}. \quad (48)$$

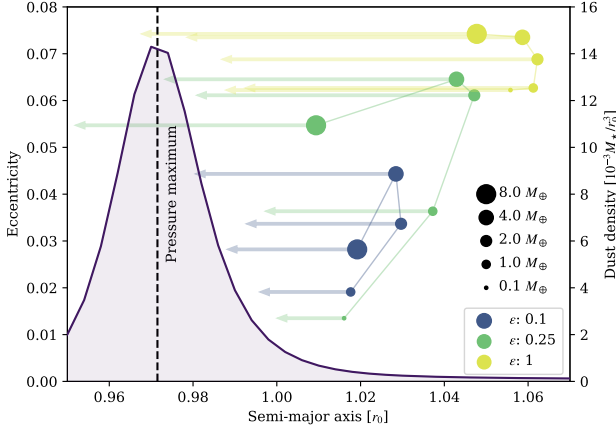


Figure 14. Location of the right fixed points. The curve shows the midplane dust density. The arrows to the left indicate the location of the periastron $a(1 - e)$. Most periastron distances fall where the dust density is a sizeable fraction of its peak value.

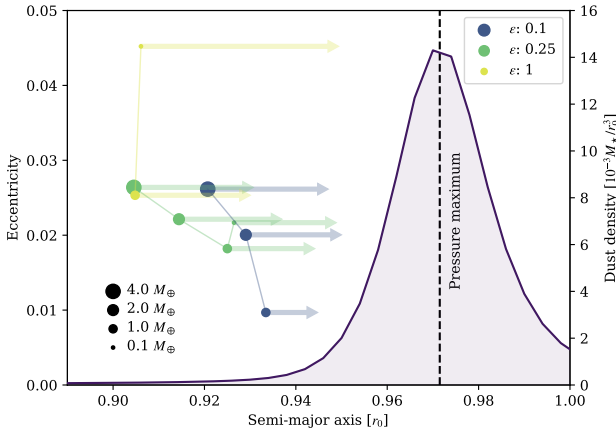


Figure 15. Same as Fig. 14 for the left fixed points. The arrows indicate this time the location of the apoastron $a(1 + e)$. Contrary to Fig. 14, the apoastron locations stay away from the peak, and at the closest distance of approach (that of the $2 M_{\oplus}$ planet with $\varepsilon = 0.1$), the density is $\sim 20\%$ only of the peak value.

The accretion radius has to be evaluated in the headwind regime, appropriate for an eccentric planet (e.g. [Ormel 2017](#)):

$$r_{\text{acc}} = \sqrt{\frac{2GM\tau_s}{(1/2)\varepsilon r \Omega^2}} = 2r \sqrt{\frac{q\tau_s}{e}}. \quad (49)$$

Using Eqs. (48) and (49), we can recast the diffusion time as:

$$T_{\text{diff}} = \frac{4q\tau_s}{\delta e h^2} \Omega^{-1}. \quad (50)$$

By comparison with the synodic period, we see that the “scar” is erased at the next passage of the planet if:

$$\frac{q\tau_s}{\delta h^2} < \pi \quad \text{or} \quad \frac{q}{h_d^2} < \pi. \quad (51)$$

This condition simply consists of a comparison between the planet-to-star mass ratio and the square of the aspect ratio of the dusty disc. With our parameters, it translates into:

$$q \lesssim 7 \times 10^{-5} \quad \text{or} \quad M \lesssim 26 M_{\oplus}. \quad (52)$$

This mass limit is above the threshold for runaway gas accretion. The vertical cut of dust density for an $8 M_{\oplus}$ planet displayed in Fig. 13 shows that the dust is lifted off the midplane. The time it takes for the dust particles to settle back toward the midplane is $\sim (\Omega_K \tau_s)^{-1}$, which for our choice of the Stokes number amounts to 16 orbital periods, comparable to the synodic period for a planet with an eccentricity comparable to the gaseous disc’s aspect ratio.

It is therefore reasonable to consider that, in our ring, a rocky protoplanetary core essentially accretes from an unperturbed dusty ring at each incursion. If the diffusion parameter δ is smaller, or if the dimensionless stopping time of the pebbles is larger, the dusty disc may be much thinner and the mass limit may be significantly smaller. It would then be necessary to take into account the fact that the planet accretes from a dusty disc significantly perturbed by its previous passages. Figs. 12 and 13 reveal mild perturbations of the ring away from the planet, especially in the case of an $8 M_{\oplus}$ planet. In these simulations, however, the setup has an azimuthal period of 1.6 rad, which entails a shorter synodic period and less time for the ring to relax toward the unperturbed configuration between two successive incursions of the planet.

The diffusion time τ_{ring} of the dust across the ring is relatively short. Using Eq. (37) and the fact that $w_g \gtrsim H$, we obtain $\tau_{\text{ring}} \sim w_d^2 / (\delta H^2 \Omega_K) \gtrsim (\tau_s \Omega_K)^{-1}$, comparable to the vertical settling time. This timescale being much shorter than that of accretion, if the ring is not fed from outside by an inward flux of pebbles, the surface density of dust decays uniformly while keeping a profile similar to the initial one. The fixed points move to adjust to the slowly varying surface density of the ring, and, as long as they exist, the planet keep feeding from the ring. We remark that the impact of the decrease of the ring’s surface density on the position of the fixed points should be exactly the same as that of the decrease of ε presented in section 4.3: the fixed points should move toward the ring. The trapping on an eccentric orbit ceases when the dust density is low enough that the planet’s luminosity becomes subcritical and its eccentricity is damped. The whole process should be studied (i) either via long-term numerical simulations at intermediate resolution (the resolution used in the present study does not allow simulations over thousands of orbits over a reasonable timescale) possibly with a different prescription for dust accretion than the one used here, as coarser cells near the planet may be larger than its effective accretion radius; (ii) or in a semi-analytical manner, by tracking the evolution of the azimuthally averaged dust density in the ring.

We comment that the synodic period of the planet with respect to the location of the ring where the accretion rate peaks is relatively short ($\gtrsim 10$ orbits) compared to the timescale of the variations of semi-major axis and eccentricity ($\sim 10^2$ orbits). Consequently, if there are azimuthal variations of the dust surface density along the ring (hence variations of the peak luminosity and thermal force from one incursion to the next), their impact on the orbital evolution of the planet should average out and the trapping process should be broadly similar to that for an axisymmetric dust ring. We therefore expect a dust ring subjected to the RWI ([Lovelace et al. 1999](#); [Li et al. 2000](#)) or the dusty RWI ([Liu & Bai 2023](#)) to trap rocky planets on eccentric orbits. For the same reason we expect that the trapping mechanism would essentially be unchanged should the ring be mildly perturbed from previous incursions of the planet.

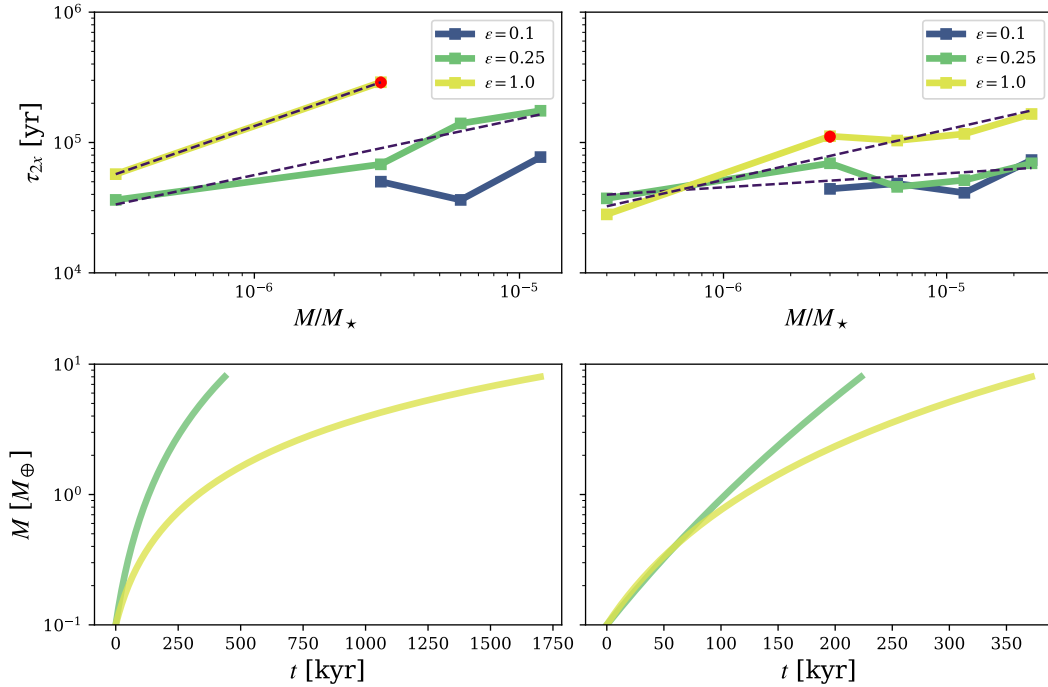


Figure 16. Top row: mass doubling time as a function of planetary mass at the inner (left) and outer (right) fixed points. Bottom row: planetary mass as a function of time, for a planet trapped at the inner fixed point (left) or at the outer fixed point (right). These time dependencies are analytical estimates obtained from the fits of the mass doubling time, shown with dashed lines in the first row. We do not provide a dependence for the case $\varepsilon = 0.1$, for which we do not have the lowest mass $M = 0.1 M_{\oplus}$.

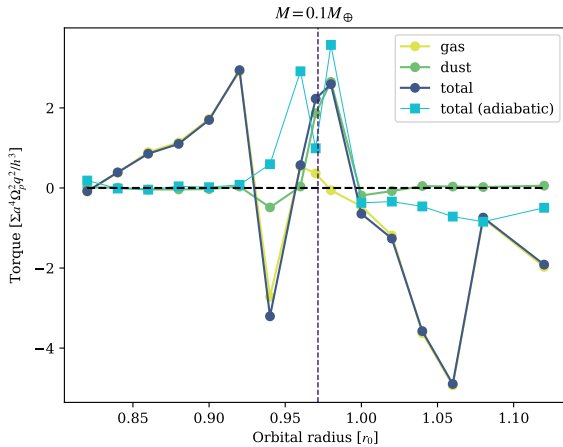


Figure 17. Normalised torque exerted on a non-luminous low-mass embryo near the ring. The gas dominates the total torque, except within the ring where the dust nearly accounts for all the torque. The thin line with squares shows the total torque when the gas is adiabatic.

5.3 Ring expansion

The process presented here relies almost exclusively on thermal torques, as discussed in length in section 2. The usual resonant torques (Lindblad and corotation) are immaterial for the trapping. All what matters is that the planet can feed from a radially narrow distribution of dust, in order to have a significantly variable luminosity. For the needs of the present study, we realised this radially

narrow dust ring by trapping dust within a pressure bump, but *per se* the pressure bump is not required for the trapping at the outer orbit to take place, as mentioned in section 4.2. It should also occur in the clumpy rings proposed by [Jiang & Ormel \(2021\)](#), which have sharp edges (at least on their outer edge). A remarkable property of these rings is their trend to expand with time. Could a planet trapped on an eccentric orbit by such a ring follow its expansion, or would it be left in place? A planet that would follow the ring's expansion would no longer have $(\dot{a}, \dot{e}) = (0, 0)$. In the frame comoving with the ring, a steady state would be achieved for $(\dot{a}, \dot{e}) = (\dot{r}_{\text{ring}}, 0)$. The location of the planet on the $\dot{e} = 0$ contour would then be given by the intersection of the $\dot{e} = 0$ contour and that with $\dot{a} = \dot{r}_{\text{ring}}$, if it exists. For an Earth-mass object trapped on an outer orbit, we read in Fig. 5 that the maximal achievable drift rate on the $\dot{e} = 0$ contour would be of order of $10^{-4}(GM_{\star}/a)^{1/2}$. This corresponds to $\dot{a}_{\text{max}} \approx 2 \times 10^{-4} \text{ au.yr}^{-1} = 200 \text{ au.Myr}^{-1}$. This maximal rate should be compared to the expansion rates found by [Jiang & Ormel \(2021\)](#). They find a particularly fast expansion for a ring formed at 10 au (their Fig. 12), with an initial rate $\lesssim 50 \text{ au.Myr}^{-1}$, while their Tab. 1 reports drift velocities that are all below this maximal rate (in general by more than one order of magnitude, and marginally for one of them). Naturally, the characteristics of these rings differ from those of the ring considered in this study, but given the considerable margin we find even for our lightweight ring ($10 M_{\oplus}$), the mechanism we report here should allow expanding clumpy rings to easily transport growing planets to several tens of astronomical unit over timescales $\gtrsim 1 \text{ Myr}$, provided the mechanism unveiled here remains efficient at larger orbital distances.

This discussion begs the question of how far from the star can the trapping mechanism operate. It essentially boils down to a comparison of the planet's luminosity achievable at a given distance to

the local value of the critical luminosity, given by Eq. (2). When the former is much larger than the latter, the thermal forces at the passage during the ring dominate the dynamical evolution of the planet. For a planet of given mass, given eccentricity and for a given Stokes number, the accretion radius scales with the orbital distance of the planet r , while the planet-dust relative speed scales with $r^{-1/2}$. The luminosity achievable therefore scales with $r^{1/2-\alpha_r}$ regardless of whether accretion is in the 2D or 3D regime, where α_r is a slope of surface density similar to that introduced in section 3.2, describing how the dust surface density in the rings vary with radius. The critical luminosity itself scales with two key quantities, that have opposite behaviour with radius: the thermal diffusivity, which increases outwards, and the density of the gas at the midplane (which decreases outwards). The thermal diffusivity depends itself on the temperature, density and opacity as described by Eq. (29). Assuming the latter scales as $\rho^0 T^2$ (Bell & Lin 1994), the critical luminosity scales as $r^{3f+\alpha}$, where f is the disc's flaring index $\partial \log h / \partial \log r$. The ratio of the planet's achievable luminosity to the critical one therefore scales as $r^{1/2-\alpha_r-\alpha-3f}$. Unless the decay of surface density in the rings is very shallow and the disc has little flaring, this quantity decreases with radius and the mechanism presented should cease to operate at some distance from the central object. We have seen that by reducing the luminosity by a factor of ten, the trapping is still active. If we therefore take a factor of ten as a conservative estimate, and scale the properties of the ring considered here, we infer that the trapping would become inefficient, for a nominally luminous planet with $\varepsilon = 1$, at a radius $r_c \sim 10[\text{au}] \times 10^{1/(3f+\alpha_r+\alpha-1/2)}$. As an example, if $\alpha = \alpha_r = 1/2$ and $f = 0.25$, this expression yields $r_c \sim 63$ au., while if $\alpha = \alpha_r = 1$ and $f = 0.25$, it yields $r_c \sim 28$ au. Note, however, that the dust of a given size has a larger Stokes number at larger distance from the star (Drażkowska 2014). We noticed in section 3.1 that larger Stokes numbers are more favourable to the trapping mechanism. This could allow the mechanism to operate at distances significantly larger than the limits quoted above.

5.4 Comparison to previous work

In recent years, there has been a substantial amount of work on the formation of planets in dust rings. Morbidelli (2020) considers the growth of initially Mars-sized embryos in the vicinity of dusty rings at pressure bumps, both at large distance from the central object (75 au) and at small distance (5 au). Guilera et al. (2020) consider the growth of planetesimals and planets in a pressure bump at the ice line (3 au). Chambers (2021) considers the formation of planets in several, fixed pressure bumps with radii in geometric sequence, starting from pebble accreting planetesimals, all the way to gas accreting, large mass planets. Lau et al. (2022) study the formation of rocky cores at pressure bumps, both relatively close to (~ 14 au) and far from (~ 100 au) the central object, starting from dust coagulation and drift. Jiang & Ormel (2023) study planet formation in dusty rings, starting from the formation of planetesimals, which subsequently accrete pebbles. These authors do not limit themselves to dust rings at pressure bumps, unlike previous studies, and also incorporate results about the formation of planets in clumpy rings (Jiang & Ormel 2021), which do not rely on the presence of a pressure maximum. Broadly, these results show that the assembly of rocky cores with a mass sufficient to trigger runaway gas accretion occurs on timescales shorter than lifespan of the disc in the inner disc ($r \lesssim 10$ au), while the results are more nuanced in the outer disc ($r = O(10^2)$ au). Morbidelli (2020) finds unlikely the build up of critical mass cores at 75 au, essentially because the cores carve a gap in the dust and have their accretion rate limited by the dust

diffusion. Chambers (2021) subsequently argues that the moderate eccentricity of the cores, in addition to their finite accretion radius, allow them to explore a more extended region, thereby increasing their accretion rates. Some of their calculations show indeed giant planet at large distances. Lau et al. (2022) obtain critical mass cores on short timescales (of the order of 100 kyr) even at large distances from the star, while Jiang & Ormel (2023) similarly obtain $10 M_\oplus$ cores in clumpy rings at 75 au, on timescales shorter than 1 Myr. Crucial to the outcome is the torque exerted on the planet during the phase from 1 to $10 M_\oplus$. In this respect, these studies share many similarities. They only consider the torque exerted by the gas and discard that from the dust. The latter, however, has been shown to be potentially important even in smooth discs (Benítez-Llambay & Pessah 2018; Guilera et al. 2023), and is dominant in pressure bumps (Pierens & Raymond 2024, and the present work — section 5.1). The torque from the gas is computed from an *ad hoc* density profile for the pressure bump, which is in general Gaussian. Several degrees of accuracy are considered. Some authors use the torque formulae for locally isothermal discs obtained for discs with power law profiles of surface density and temperature, and inject in these formulae the rapidly varying slopes of surface density and temperature within the bump to obtain torque expressions. Others consider non-isothermal effects and the saturation of the corotation torque, for which they use more sophisticated torque formulae (Paardekooper et al. 2011; Jiménez & Masset 2017), or a variant (Chambers 2021) in which non-isothermal effects are accounted for (Paardekooper et al. 2010), but not the saturation of the corotation torque. The migration path of the planets is then bracketed between that obtained with such prescription, and one obtained from the Lindblad torque only, corresponding to a fully saturated corotation torque. Taking into account the saturation of the corotation torque (i.e., its trend to decay towards a small value) is of particular importance: the Lindblad torque alone cannot halt migration, as it is invariably negative (D'Angelo & Lubow 2010), even at pressure bumps (Masset 2011). The corotation torque is therefore required to obtain a planet trap, but this can only happen if it is not saturated. Unless the turbulence is very weak (i.e. the effective viscosity is very low), a significant corotation torque should subsist for protoplanets with masses up to that of critical mass cores ($\sim 10 M_\oplus$), but the degree of saturation of the torque regulates the location of the trap with respect to the peak of dust and ultimately the accretion rate of pebbles (Morbidelli 2020). In addition to the Lindblad and corotation torque, the planet is subjected to thermal torques. Guilera et al. (2020) include these torques, but assume the planet to be on a circular orbit independently of whether its luminosity is sub- or super-critical, and they abruptly set thermal torques to zero passed the relatively small critical mass

$$M_c = \frac{\chi c_s}{G}. \quad (53)$$

As a consequence of their assumption of a circular orbit, they cannot observe the effects we report here. An additional effect not taken into account in these studies is the role played by dynamical corotation torques (Paardekooper 2014; Pierens 2015) on the rocky cores, or their higher mass version (Masset & Papaloizou 2003). As there seems to be a shift of paradigm toward laminar discs dominated by magnetised winds (Bai & Stone 2013; Bai & Stone 2017), in which accretion is driven by magnetic torques, dynamical corotation torques can build up even on slowly or non-migrating planets (McNally et al. 2018) in the Earth mass range and completely alter their orbital evolution.

Notwithstanding the fact that a growing planet in the $O(10^{-1}) - O(10) M_\oplus$ range should be on an eccentric orbit rather than a circular one, it can be seen that the determination of the accretion rate of a

planet on a circular orbit in a dusty ring is a very complex problem, which requires a detailed knowledge of the ring profiles and of the microphysics in the ring to establish accurately the distance of the orbit to the peak of dust. This distance may be, or not, favourable to the planet growth, and a given scenario of growth and migration is inherently uncertain anyway due to the neglect of dynamical corotation torques.

The mechanism we present here is completely immune to these issues. It occurs whenever the dust density has relatively narrow radial variations, it is virtually independent of Lindblad's and corotation torques, and allows for a systematic consumption of the dust until the planet's luminosity becomes subcritical. The question of the location of the orbit becomes that of the location of the periastron (or apoastron), and that location is precisely dictated by the concentration of dust, rather than by the subtle balance of resonant torques from the gas.

Very recently, [Chrenko & Chametla \(2023\)](#) investigated the evolution of low-mass planets near pressure bumps. Those with subcritical luminosities, predicted to be trapped near the pressure local maximum ([Masset 2017](#)), are indeed found to remain at the pressure bump. Once their luminosity becomes supercritical, they become eccentric. However, their luminosity is kept constant, rather than being modulated according to the underlying dust density. Owing to the lack of variation of the heating force along their epicycle, they suffer the fate described in section 2: they migrate inwards and escape the ring. [Pierens & Raymond \(2024\)](#) studied the growth and orbital evolution of low-mass planets at pressure bump through extensive two-dimensional simulations, which allow much longer integrations than our three-dimensional simulations with nested meshes. They release the accretional luminosity to the gas in the vicinity of the planet, and have a realistic prescription for the accretion of dust, modelled as a pressureless fluid. These prescriptions allow for a variation of the luminosity (and heating force) along the orbit. They observe behaviours similar to the ones we report, which we believe to be based on the same mechanism. Namely, they observe that the planet can settle outside the ring with an eccentricity $e \sim h$ and a variable accretion rate, much larger at periastron, compatible with a planet trapped at an outer fixed point. They also find instances of an eccentric planet trapped inside the ring, such as the case without dust back-reaction on their Fig. 8. The overshoot of eccentricity, and the initial slow decay of the semi-major axis, are typical of the trajectories about the inner fixed point (see Fig. 6), and suggest that the mechanism at work in their simulations is similar in nature to the mechanism reported here. Thanks to the long-term nature of their calculations, they also observe interesting additional effects that our short runs are unable to capture, such as the formation of a dust-vortex and its interaction with the planet, which warrants further work.

5.5 Caveats of our analysis

We draw here a non-comprehensive list of the caveats of the present analysis.

5.5.1 Only one, non-inclined planet

In the present work, we have considered only one planet at a time, assumed to be coplanar with the disc. If there is indeed only one planet, the assumption of coplanarity is a reasonable one: [Eklund & Masset \(2017\)](#) have found that the eccentricity grows $\sim 3\times$ times faster than inclination, and that once the eccentricity reaches significant levels (larger than λ/a), the growth of inclination stops, so that the inclination remains at a very small value. However, if various embryos

with super-critical luminosity are simultaneously present on the same side of the ring (either inside or outside), they may undergo close encounters which will change their eccentricity and inclination. The evolution of an embryo with an inclination larger than the aspect ratio of the dusty disc depends on the argument of periastron: if the latter is close to 0 or 180° (i.e. if it lies near the line of nodes), the planet goes through the dust at periastron, and effects similar to those described here should occur. The dynamics in this case warrants further study as the introduction of a new degree of freedom, the inclination, may lead to significant changes with respect to the scenario of a coplanar planet. If the line of nodes and periape are misaligned, the planet does not accrete significantly on any part of its orbit. Its luminosity drops and, if it becomes sub-critical, the inclination and eccentricity are damped. The subcritical planet should then resume a migration toward the ring ([Chrenko & Chametla 2023](#)), until it accretes a sufficient amount of dust to repeat the whole process of convergence toward the fixed point in (a, e) .

5.5.2 No feed back of the dust

In this exploratory work we have not considered the feed back of the dust onto the gas in the present work. The dust to gas ratio near the centre of the ring suggests that the dust feedback onto the gas, which is neglected in the present analysis, may play a role. The streaming instability could set in, and the formation of planetesimals could occur in the ring. We do not take into account this process, nor the accretion of planetesimals, in our analysis. [Pierens & Raymond \(2024\)](#) find that embryos follow different paths depending on whether the feed back is included. The inclusion of feed back should be important in determining the dust torque while the planet has a small eccentricity. When the planet has a sizeable eccentricity and is near a fixed point, the feed back should not have a strong impact on the net force, then dominated by the thermal force. We do not address either the question of the life expectancy of the ring, which is beyond the scope of this paper. Should the lifetime of a ring be shorter than the time it takes for the planet to accrete most of its mass, the trapping mechanism envisioned here would stop, as the accretion rate would drop below the levels required to counteract migration. If the residual accretion rate drops below that corresponding to the critical luminosity of the planet (Eq. 2), its eccentricity would decay and its inwards migration would resume. However, given that most discs do exhibit several rings at a given time ([Huang et al. 2018](#)), it could approach another ring from the outside and end up trapped on the outer side, resuming accretion, unless there is no ring inside to prevent its migration. This hypothetical scenario underlines that planet's growth and orbital evolution is tightly linked to the evolution of the rings, not only because they feed from them, but also because their evolutionary path strongly depends on the time behaviour of the rings' radii and their life expectancy.

5.5.3 No cut-off of the pebble accretion

There is a variety of effects that may limit the ability of the planet to accrete pebbles which have not been taken into account in our approach. Our accretion procedure, which removes pebbles from the 8 zones nearest to the planet, does not consider the turbulent stirring that may inhibit the settling of a fraction of the dust content.

Planets with eccentricities larger than the disc's aspect ratio have a supersonic motion with respect to the gas on the radial parts of their epicycle, and have therefore a bow shock. Pebbles crossing the bow shock may be destroyed ([Liu & Ormel 2018](#)). We do not take

this effect into account. Note however that in most cases the planet does barely accrete except at peri- or apoastron. At those locations, its velocity with respect to the gas is half the velocity it has when it crosses the circle of radius equal to the semi-major axis, so that it would have a supersonic motion at peri- or apoastron only for $e > 2h$. This implies that the upper part of the \dot{e} and \dot{a} maps presented in section 4.1 may be different, but not the main part, for $e < 0.1$ (our disc has $h = 0.05$). In particular, all the fixed points we have found have an eccentricity below $2h$ (see Figs. 14 and 15), so they should not be affected by this effect.

One dimensional calculations of the structure of a pebble accreting planetary envelope show that pebbles do not hit directly the core above a fraction of an Earth mass (Brouwers et al. 2018). Instead, they vaporise before reaching the core and form a high metallicity envelope around the core. The energy release is then smaller than that given by Eq. (42). The reduction factor for the luminosity that we introduced in section 4.3 is an *ad hoc* attempt to take this effect into consideration. However, further complications come into play: part of the envelope may be recycled by gas flowing in and out of the Bondi sphere (Ormel et al. 2015; Fung et al. 2015), which may limit the core's growth (Brouwers et al. 2021). Besides, the rate of recycling increases with the planetary eccentricity (Bailey et al. 2021). Much further work is therefore needed to assess to which extent an eccentric planet retains its high metallicity envelope. Regardless of the planet's eccentricity, results obtained from calculations with a steady flow of pebbles may differ substantially from results obtained when the flow of pebbles is intermittent, as is the case for the mechanism presented here. In addition, our numerical scheme implies that the heat released by accretion is injected instantaneously in the eight cells surrounding the planet. While the diffusion timescale of the heat within the hot trail is a small fraction of the orbital timescale in the headwind regime (Eklund & Masset 2017) and is properly accounted for by our numerical scheme, the delay of heat transfer from the planet to the immediately surrounding cells involves several phases: the emergence of heat from the convective zone, and its subsequent transfer by radiation up to the distance of the neighbouring cell centres. Assessing this delay should be done with a specific, time-dependent study of pebble accretion down to the core scale.

Finally, our study cannot capture properly the dynamics of the planet when its mass exceeds the pebble isolation mass (PIM). The latter indeed requires that a local pressure maximum be created on the outer side of the orbit. However, the time it takes for this maximum to appear is larger than the 3-orbit duration of our runs. We comment that the PIM has been studied for the case of eccentric planets (Chametla et al. 2022) when there is a steady flow of pebbles originating from the outer disc. Here, there is rather a given reservoir of pebbles already in the ring from which the planet accretes. Whether and how accretion proceeds once the planet's mass exceeds the PIM should be the subject of future studies. Also, we mention that Sándor & Regály (2021) found that the PIM is significantly increased at pressure bumps, so the largest mass of our numerical study may well be significantly below the isolation mass.

5.5.4 Other limitations

In addition to the caveats listed above, we mention that our analysis considers only one value for the Stokes number ($\tau_s = 0.01$) and one value for the turbulence parameter ($\alpha_v = 10^{-4}$). Pierens & Raymond (2024) consider rings with different Stokes number and find that the accretion spikes near perihelion are shorter and higher when $\tau_s = 0.1$, as can be expected for the more narrow dusty rings obtained in that case. They find that planets in that case as subjected

to a similar trapping than those of the case $\tau_s = 0.01$, but have a mass that saturate at smaller values. They also perform simulations with $\tau_s = 10^{-3}$, in which the ring has a width marginally larger than the aspect ratio of the gas, which show a trapping similar to that obtained with larger Stokes numbers, but for which planets undergo a much slower growth.

We also add neither the mass nor the momentum accreted from the dust to the planet. Over the very short timescales of our run, the mass accreted is extremely small and neglecting it is legitimate. As for the momentum of the dust, we expect that it would change in a sizeable manner the orbital parameters of the planet when the mass accreted is comparable to the mass of the planet. Since the timescales for the evolution of eccentricity are at least one order of magnitude shorter than the mass doubling times, the impact of the accreted momentum on the evolution of eccentricity should be subdominant compared to that of the thermal forces.

6 CONCLUSIONS

We study the orbital evolution of a planetary embryo forming in a dusty ring of $10 M_\oplus$ at 10 au from a solar mass star. We take into account the accretion of dust and the radiative feedback on the gaseous disc: the energy released by accretion is used to heat the nearby gas. Even at the starting mass of our study ($0.1 M_\oplus$), embryos are found to be sufficiently luminous to have their eccentricities excited. After undergoing eccentricity growth, they end up trapped in one of these two stable orbits: an orbit outside the ring, with a periastron in the ring, at which the planet accretes at each passage, or an orbit inside the ring, with its apoastron slightly interior to the ring, so that the planet accretes significantly less on this orbit than on the first one. A critical mass core can be assembled in a fraction of a Myr on the outer orbit, while the core may remain subcritical over the disc lifespan on the inner orbit. The eccentricity of the outer orbit is comparable to the aspect ratio of the gaseous disc and the eccentricity of the inner orbit is smaller, typically by a factor of two. Which of the two orbits is eventually reached by growing cores depends on the starting point of the embryo in the ring. The watershed between inner and outer tracks is close to the peak of dust density, hence an accurate value of the torque exerted on a low-mass embryo prior to its eccentricity growth is required to determine whether it will eventually join the inner or the outer orbit. Our model tends to favour the outer orbit, but it is likely that the preferred orbit depends on the specifics of the ring, or even on the exact time at which the growth of eccentricity starts, as the torque exerted by the dust and gas in a low-viscosity disc may have a stochastic component. The trapping at the outer point relies on a vigorous heating force at periastron, arising from the high accretion rate of the planet on this portion of its orbit. This force has same direction as the planet's motion, and increases the planet's angular momentum and orbital energy. This increase at periastron compensates the variation of these two quantities over the rest of the orbit. The variation of the planet's luminosity as a function of the orbital phase is therefore a key ingredient for the trapping on the outer orbit. The trapping at the inner point is also based on thermal forces, but details differ: the planet adopts the eccentricity at which its migration changes sign. At an adequate distance from the ring, this eccentricity turns out to be constant in time. A much milder modulation of the planet's luminosity as a function of the orbital phase is required for a trapping on the inner orbit, which is why the planet never approaches the dust as much as on the outer orbit. There is a considerable leeway for our mechanism to operate. Even when we arbitrarily reduce the accretion luminosity by a factor

of ten, we still find an outer and inner eccentric trapping orbit. Since the existence and location of the outer orbit is precisely based on the accretion of dust, the planet is *de facto* a dust hunter, and consumes the ring in a systematic fashion. The trapping mechanism at the outer orbit does not rely on the existence of a pressure bump (we did set up one, to give rise to a dust ring, but this is not necessary for the trap to exist). It occurs whenever the dust has a radially narrow distribution. It should therefore occur in the clumpy rings described by [Jiang & Ormel \(2021\)](#). An interesting prospect is that these rings can expand with time. As they do, so does the outer trapping orbit: these rings can bring forming planets to several tens of astronomical units over Myr timescales. The present work suggests that as long as protoplanets in the Earth-Neptune mass range are accreting, even weakly so, their eccentricities are driven by the disc rather than damped. [Laune et al. \(2022\)](#) find evidence for such driving in the apsidal alignment of resonant transiting pairs. A necessary and significant step forward to make more accurate predictions about the accretion of dust by an eccentric planet would be a small scale description of pebble accretion, down to the core, in a time varying flow with a time varying pebble input. This would allow us to better estimate the value of the planet's luminosity.

ACKNOWLEDGEMENTS

The authors wish to thank the referee, R. O. Chametla, for comments that led to an improvement of this manuscript, and O. Chrenko for his insightful feedback. The simulations included in this work were executed on the Stellar and Della clusters at Princeton University as well as the Piz-Daint cluster at CSCS under the project s1077. F. M. acknowledges support from UNAM's grant PAPIIT 107723, UNAM's DGAPA PASPA program and the Laboratoire Lagrange at Observatoire de la Côte d'Azur for hospitality during a one-year sabbatical stay. P. B. L. acknowledges support from ANID, QUIMAL fund ASTRO21-0039 and FONDECYT project 1231205.

DATA AVAILABILITY

The FARGO3D setup used in the present work will be shared upon reasonable request to the corresponding author.

REFERENCES

Ataiee S., Kley W., 2020, *A&A*, **635**, A204
 Bai X.-N., Stone J. M., 2013, *The Astrophysical Journal*, **769**, 76
 Bai X.-N., Stone J. M., 2017, *ApJ*, **836**, 46
 Bailey A., Stone J. M., Fung J., 2021, *The Astrophysical Journal*, **915**, 113
 Baruteau C., Masset F., 2008, *ApJ*, **678**, 483
 Bell K. R., Lin D. N. C., 1994, *ApJ*, **427**, 987
 Benítez-Llambay P., Masset F. S., 2016, *ApJS*, **223**, 11
 Benítez-Llambay P., Pessah M. E., 2018, *ApJ*, **855**, L28
 Benítez-Llambay P., Masset F., Koenigsberger G., Szulágyi J., 2015, *Nature*, **520**, 63
 Benítez-Llambay P., Ramos X. S., Beaugé C., Masset F. S., 2016, *ApJ*, **826**, 13
 Benítez-Llambay P., Krapp L., Pessah M. E., 2019, *ApJS*, **241**, 25
 Béthune W., Lesur G., Ferreira J., 2017, *A&A*, **600**, A75
 Brouwers M. G., Vazan A., Ormel C. W., 2018, *A&A*, **611**, A65
 Brouwers M. G., Ormel C. W., Bonsor A., Vazan A., 2021, *A&A*, **653**, A103
 Chambers J., 2021, *ApJ*, **914**, 102
 Chametla R. O., Masset F. S., Baruteau C., Bitsch B., 2022, *MNRAS*, **510**, 3867

Chang E., Youdin A. N., Krapp L., 2023, *ApJ*, **946**, L1
 Chrenko O., Chametla R. O., 2023, *MNRAS*, **524**, 2705
 Chrenko O., Brož M., Lambrechts M., 2017, *A&A*, **606**, A114
 Cornejo S., Masset F. S., Chametla R. O., Fromenteau S., 2023, *MNRAS*,
 D'Angelo G., Lubow S. H., 2010, *ApJ*, **724**, 730
 Drązkowska J., 2014, PhD thesis, Ruprecht-Karls University of Heidelberg, Germany
 Drązkowska J., Alibert Y., 2017, *A&A*, **608**, A92
 Dullemond C. P., et al., 2018, *ApJ*, **869**, L46
 Eklund H., Masset F. S., 2017, *MNRAS*, **469**, 206
 Fendyke S. M., Nelson R. P., 2014, *MNRAS*, **437**, 96
 Flaherty K., et al., 2020, *ApJ*, **895**, 109
 Fromang S., Nelson R. P., 2005, *MNRAS*, **364**, L81
 Fromenteau S., Masset F. S., 2019, *MNRAS*, **485**, 5035
 Fung J., Artymowicz P., Wu Y., 2015, *ApJ*, **811**, 101
 Guilera O. M., Sándor Z., Ronco M. P., Venturini J., Miller Bertolami M. M., 2020, *A&A*, **642**, A140
 Guilera O. M., Benítez-Llambay P., Miller Bertolami M. M., Pessah M. E., 2023, *ApJ*, **953**, 97
 Huang J., et al., 2018, *ApJ*, **869**, L42
 Jennings J., Booth R. A., Tazzari M., Clarke C. J., Rosotti G. P., 2022, *MNRAS*, **509**, 2780
 Jiang H., Ormel C. W., 2021, *MNRAS*, **505**, 1162
 Jiang H., Ormel C. W., 2023, *MNRAS*, **518**, 3877
 Jiménez M. A., Masset F. S., 2017, *MNRAS*, **471**, 4917
 Krapp L., Gressel O., Benítez-Llambay P., Downes T. P., Mohandas G., Pessah M. E., 2018, *ApJ*, **865**, 105
 Kretke K. A., Lin D. N. C., 2007, *ApJ*, **664**, L55
 Lau T. C. H., Drązkowska J., Stammer S. M., Birnstiel T., Dullemond C. P., 2022, *A&A*, **668**, A170
 Laune J. T., Rodet L., Lai D., 2022, *MNRAS*, **517**, 4472
 Lega E., Crida A., Bitsch B., Morbidelli A., 2014, *MNRAS*, **440**, 683
 Li H., Finn J. M., Lovelace R. V. E., Colgate S. A., 2000, *ApJ*, **533**, 1023
 Liu H., Bai X.-N., 2023, *MNRAS*, **526**, 80
 Liu B., Ormel C. W., 2018, *A&A*, **615**, A138
 Lovelace R. V. E., Li H., Colgate S. A., Nelson A. F., 1999, *ApJ*, **513**, 805
 Masset F. S., 2011, *Celestial Mechanics and Dynamical Astronomy*, **111**, 131
 Masset F. S., 2017, *MNRAS*, **472**, 4204
 Masset F. S., Benítez-Llambay P., 2016, *ApJ*, **817**, 19
 Masset F. S., Papaloizou J. C. B., 2003, *ApJ*, **588**, 494
 Masset F. S., Velasco Romero D. A., 2017, *MNRAS*, **465**, 3175
 McNally C. P., Nelson R. P., Paardekooper S.-J., 2018, *MNRAS*, **477**, 4596
 Morbidelli A., 2020, *A&A*, **638**, A1
 Muto T., Takeuchi T., Ida S., 2011, *ApJ*, **737**, 37
 Ormel C. W., 2017, in Pessah M., Gressel O., eds, *Astrophysics and Space Science Library* Vol. 445, Formation, Evolution, and Dynamics of Young Solar Systems. p. 197, doi:10.1007/978-3-319-60609-5_7
 Ormel C. W., Shi J.-M., Kuiper R., 2015, *MNRAS*, **447**, 3512
 Paardekooper S.-J., 2014, *MNRAS*, **444**, 2031
 Paardekooper S., Baruteau C., Crida A., Kley W., 2010, *MNRAS*, **401**, 1950
 Paardekooper S., Baruteau C., Kley W., 2011, *MNRAS*, **410**, 293
 Pierens A., 2015, *MNRAS*, **454**, 2003
 Pierens A., 2023, *MNRAS*, **520**, 3286
 Pierens A., Raymond S. N., 2024, *arXiv e-prints*, p. arXiv:2402.05760
 Pinilla P., Birnstiel T., Ricci L., Dullemond C. P., Uribe A. L., Testi L., Natta A., 2012, *A&A*, **538**, A114
 Riols A., Lesur G., 2018, *A&A*, **617**, A117
 Riols A., Lesur G., Menard F., 2020, *A&A*, **639**, A95
 Rosotti G. P., Juhasz A., Booth R. A., Clarke C. J., 2016, *MNRAS*, **459**, 2790
 Sándor Z., Regály Z., 2021, *MNRAS*, **503**, L67
 Shakura N. I., Sunyaev R. A., 1973, *A&A*, **24**, 337
 Velasco Romero D. A., Masset F. S., 2019, *MNRAS*, **483**, 4383
 Velasco Romero D. A., Masset F. S., 2020, *MNRAS*, **495**, 2063
 Velasco Romero D. A., Masset F. S., Teysier R., 2022, *MNRAS*, **509**, 5622
 Weber P., Benítez-Llambay P., Gressel O., Krapp L., Pessah M. E., 2018, *ApJ*, **854**, 153
 Whipple F. L., 1972, in Elvius A., ed., *From Plasma to Planet*. p. 211
 Youdin A. N., Lithwick Y., 2007, *Icarus*, **192**, 588

Zhang S., et al., 2018, *ApJ*, 869, L47
 Ziampras A., Kley W., Dullemond C. P., 2020, *A&A*, 637, A50

APPENDIX A: AVERAGE THERMAL TORQUE ON A PLANET OF FIXED LUMINOSITY

We assume that the corotation offset is a small fraction ϵ of the epicyclic excursion ea : $x_p^0 = \epsilon ea$, where $|\epsilon| \ll 1$ and rewrite the coordinates of the velocity w.r.t. the gas of Eq. (14) as:

$$(\dot{x}|_{\text{gas}}, \dot{y}|_{\text{gas}}) = \Omega_p ea \left[\sin(\Omega_p t), \frac{1}{2} \cos(\Omega_p t) + \frac{3}{2} \epsilon \right] \quad (\text{A1})$$

The unit vector \mathbf{n} with same direction as the planet's velocity with respect to the gas has therefore the components:

$$(n_x, n_y) = A \times \left[\sin(\Omega_p t), \frac{1}{2} \cos(\Omega_p t) + \frac{3}{2} \epsilon \right]. \quad (\text{A2})$$

with:

$$A = \frac{1}{\sqrt{\sin^2(\Omega_p t) + \left[\frac{1}{2} \cos(\Omega_p t) + \frac{3}{2} \epsilon \right]^2}} \quad (\text{A3})$$

Using the fact that $|\epsilon| \ll 1$, we expand the prefactor of Eq. (A2) as:

$$A = \frac{1}{\left[1 - \frac{3}{4} \cos^2(\Omega_p t) \right]^{1/2}} - \frac{\frac{3}{4} \epsilon \cos(\Omega_p t)}{\left[1 - \frac{3}{4} \cos^2(\Omega_p t) \right]^{3/2}} \quad (\text{A4})$$

The thermal force exerted on the planet has expression:

$$\mathbf{F} = F_d \mathbf{n}, \quad (\text{A5})$$

and (the vertical component of) its torque is:

$$\Gamma = (a+x)F_y - yF_x. \quad (\text{A6})$$

Using Eqs. (4), (A2), (A4) and (A6) we obtain:

$$\begin{aligned} \Gamma = F_d a \left\{ [1 - e \cos(\Omega_p t)] \left[\frac{1}{2} \cos(\Omega_p t) + \frac{3}{2} \epsilon \right] \right. \\ \left. - 2e \sin^2(\Omega_p t) \right\} \\ \times \left\{ \frac{1}{\left[1 - \frac{3}{4} \cos^2(\Omega_p t) \right]^{1/2}} - \frac{\frac{3}{4} \epsilon \cos(\Omega_p t)}{\left[1 - \frac{3}{4} \cos^2(\Omega_p t) \right]^{3/2}} \right\} \end{aligned} \quad (\text{A7})$$

We average this expression over one orbital period. Retaining only terms to first order in e and ϵ that do not cancel out, we obtain:

$$\begin{aligned} \langle \Gamma \rangle = F_d a e \left\langle \frac{-\frac{1}{2} \cos^2(\Omega_p t) - 2 \sin^2(\Omega_p t)}{\left[1 - \frac{3}{4} \cos^2(\Omega_p t) \right]^{1/2}} \right\rangle \\ + F_d a \frac{3}{2} \epsilon \left\langle \left[1 - \frac{3}{4} \cos^2(\Omega_p t) \right]^{-1/2} \right\rangle \\ - F_d a \frac{3}{8} \epsilon \left\langle \frac{\cos^2(\Omega_p t)}{\left[1 - \frac{3}{4} \cos^2(\Omega_p t) \right]^{3/2}} \right\rangle. \end{aligned} \quad (\text{A8})$$

Each of the averages in the above expression can be expressed in terms of the complete elliptic integrals of the first and second kind (denoted respectively \mathcal{K} and \mathcal{E}). The average factor of the first line is $-4\mathcal{E}(-3)/(2\pi) \approx -1.5420$. That of the second line is $8\mathcal{K}(-3)/(2\pi) \approx 1.3729$ and that of the third line is

$(32/3)[\mathcal{E}(-3) - \mathcal{K}(-3)]/(2\pi) \approx 2.2814$. We therefore have the following expansion:

$$\langle \Gamma \rangle = F_d a (1.2038\epsilon - 1.5420e), \quad (\text{A9})$$

which can be recast as Eq. (16).

APPENDIX B: AVERAGE THERMAL TORQUE ON A PLANET WITH VARIABLE LUMINOSITY

Using the dependence of Eq. (18), we have an extra factor $[1 - es \cos(\Omega_p t)]$ for the x - and y -components of the thermal force, hence for the torque, which has therefore the expression:

$$\begin{aligned} \Gamma = F_d a [1 - es \cos(\Omega_p t)] \left\{ [1 - e \cos(\Omega_p t)] \left[\frac{1}{2} \cos(\Omega_p t) + \frac{3}{2} \epsilon \right] \right. \\ \left. - 2e \sin^2(\Omega_p t) \right\} \\ \times \left\{ \left[1 - \frac{3}{4} \cos^2(\Omega_p t) \right]^{-1/2} - \frac{3}{4} \epsilon \frac{\cos(\Omega_p t)}{\left[1 - \frac{3}{4} \cos^2(\Omega_p t) \right]^{3/2}} \right\} \end{aligned} \quad (\text{B1})$$

The time average of this quantity to first order in e and ϵ , in addition to the terms obtained in Eq. (A8), contains the following term, which scales with s :

$$\langle \Gamma \rangle_s = -F_d a \frac{es}{2} \left\langle \frac{\cos^2(\Omega_p t)}{\left[1 - \frac{3}{4} \cos^2(\Omega_p t) \right]^{1/2}} \right\rangle \quad (\text{B2})$$

The average factor in this equation can be cast as $(8/3)[4\mathcal{K}(-3) - \mathcal{E}(-3)] \approx 0.8025$, hence

$$\langle \Gamma \rangle_s = -0.40 F_d a es, \quad (\text{B3})$$

from which we infer Eq. (19).

This paper has been typeset from a $\text{\TeX}/\text{\LaTeX}$ file prepared by the author.